

Unterschrift des Betreuers



Diplomarbeit

Investigation of the influence of the ion heat flux on access to regimes of improved energy confinement in Alcator C-Mod

Ausgeführt am Institut für
Angewandte Physik
der TECHNISCHEN UNIVERSITÄT WIEN

unter der Anleitung von

Univ.-Prof. Mag.rer.nat. Dipl.-Ing. Dr.techn. Friedrich Aumayr
und
Univ.-Doz. Dipl.-Ing. Dr.techn. Elisabeth Wolfrum

durch
Matthias Schmidtmayr
Alser Straße 27/2/8
1180 Wien

Datum

Unterschrift Student

Abstract

This thesis investigates the role of the edge ion heat flux for the transitions from L-mode to H-mode in Alcator C-Mod. Several selected discharges from the low to medium density range in C-Mod were analyzed by time dependent power balance analysis using the transport code TRANSP. The ion heat flux was calculated by adding the power from the ion cyclotron resonance heating deposited in the ion channel and the electron-ion heat exchange. These calculations showed that the surface integrated edge ion heat flux obtained just prior to L-H transition increases linearly with line average density, which agrees with previous results from AUG. It appears, as if a critical amount of heat flux per particle is necessary for the transition.

TRANSP required a variety of experimental data from several different diagnostics. The most important measurements came from Thomson scattering spectroscopy (electron temperature and density), electron cyclotron emission (electron temperature) and x-ray imaging crystal spectroscopy (ion temperature).

The comparison of the results of this thesis and previous research at AUG lead to a simple linear scaling law for the critical edge ion heat flux necessary for the transition into H-mode. Although the data from C-Mod have significantly larger error bars due to the higher densities, the data from C-Mod and AUG agree remarkably well.

Assuming that ITER will operate within its envisioned operating parameters, the scaling law projects an edge heat flux of $\approx 38 kW m^{-2}$ (or a surface integrated edge ion heat flux of $\approx 26 MW$) which is well within ITER operational possibilities.

Kurzfassung

Ziel dieser Arbeit war es, die Rolle des Ionenwärmeflusses am Plasmarand für den Übergang von L-Mode zur H-Mode an Alcator C-Mod zu untersuchen. Dafür wurden ausgewählte Plasmaentladungen mit niedrigen bis mittleren Dichten mittels zeitabhängiger Leistungsbilanz untersucht.

Berechnungen mit dem Transportcode TRANSP ergaben einen linearen Zusammenhang zwischen dem Ionenwärmefluss kurz vor dem L-H Übergang und der mittleren Plasmadichte. Dieses Ergebnis stimmt mit früheren Resultaten von AUG überein die besagen, dass ein kritischer Wärmestrom pro Teilchen für den Übergang notwendig ist. Der Ionenwärmefluss wurde unter der Annahme berechnet, dass bei thermischem Gleichgewicht die gesamte in den Ionenkanal deponierte Leistung durch den Plasmarand hinaus fließen muss. Durch das Addieren der von der Ionen-Cyclotron Resonanz Heizung in die Ionen deponierten Leistung zum Wärmefluss von Elektronen zu Ionen, wurde der Ionen-Wärmefluss berechnet.

Die deponierte Leistung und der Wärmeaustausch wurden von TRANSP berechnet, wofür einige experimentelle Messgrößen benötigt wurden. Die wichtigsten Diagnostiken für diese Berechnungen waren Thomson-Streuungs-Spektroskopie (Elektronen Temperatur und Dichte), Electron-Cyclotron-Emissions Spektroskopie (Elektronen Temperatur) und X-Ray Imaging Crystal Spektroskopie (Ionen Temperatur). Der Vergleich mit den Ergebnissen von AUG führte zu einer einfachen Formel für den kritischen Ionenwärmefluss am Plasmarand für L-H Übergänge. Obwohl C-Mod wesentlich höhere Dichten hat als alle anderen Tokamaks, stimmen die Ergebnisse erstaunlich gut mit denen von AUG überein.

Für die geplanten ITER Parameter kann man mit der gefunden Formel einen ungefähren kritischen Ionenwärmestrom für L-H Übergänge im Bereich von $\approx 38 kW m^{-2}$ prognostizieren. Die etwas handlichere Größe des oberflächenintegrierten Ionenwärmestroms am Plasmarand ergibt $\approx 25 MW$, was sich direkt mit der geplanten ITER Heizleistung vergleichen lässt, die diesen Wert weit übersteigt.

Acknowledgements

The main part of this thesis was conducted at the Plasma Science Fusion Center of the Massachusetts Institute of Technology. I was only able to get the scholarship necessary for my visit to MIT because of Prof. Aumayr's recommendation and his willingness to supervise my thesis even though I was conducting most of it in the US and Germany. I'm very grateful for this opportunity! I would also like to thank Dr. Elisabeth Wolfrum from the Max-Planck-Institut für Plasmaphysik in Garching for establishing the connection to MIT, as well as her advice and feedback during the whole duration of my thesis.

Additionally I would like to thank Dr. Francois Ryter for helping me prepare for MIT, supporting me with his profound understanding of the physics of L-H transitions and encouraging me, when I had doubts about my work. My advisor at MIT was Dr. Jerry Hughes, whose door was always open whenever I ran into a problem, or had a question about my research. I am grateful for his continuous support and his very valuable comments on this thesis.

My sincere thanks also goes to Nathan Howard, Giovanni Tardini and Alex Creely for their help with TRANSP, Norman Cao for his help with HIRESR and the entire C-Mod team for their excellent work.

I would also like to thank the Austrian Marschall Plan Foundation for granting me the fellowship which made this thesis possible.

And finally I would like to thank my parents, not just for their support during my thesis, but also for their support and help during my entire student life. I could not have done it without them!

List of acronyms

AUG ASDEX Upgrade

C-Mod Alcator C-Mod

D Deuterium

ECE Electron cyclotron emission

ELM Edge localized mode

HIREXSR high resolution x-ray spectrometer with spatial resolution

ICRH Ion cyclotron resonance heating

ICRF Ion cyclotron resonance frequency

T Tritium

TS Thomson scattering

B_T Toroidal magnetic field

E_r Radial electric field

I_p Plasma current

n_s Density of species s

\bar{n}_e Line averaged electron density

P_{L-H} L-H power threshold

P_s Power; index usually describes either the power source (i.e. ohm) and/or species

$p_{s,ich}$ ICRH power deposition of species s

p_i Main ion pressure

Q_s Surface integrated heat flux of species s

q_s Heat flux of species s

R	Major radius
R_{DT}	Fusion reaction rate for deuterium and tritium
r/a	Radius normalized to magnetic axis
ρ_{tor}	Toroidal flux surface normalized radius
T_s	Temperature of species s
t_{LH}	L-H transition time
ω_c	Cyclotron frequency

Contents

1	Introduction	1
1.1	Basic Principle of Nuclear Fusion	1
1.1.1	Particle movement inside a magnetic field	3
1.1.2	Particle movement in crossed electric and magnetic fields	4
1.2	The Tokamak	5
1.2.1	Flux surfaces and flux based coordinates	7
1.3	Alcator C-Mod	9
1.4	ASDEX Upgrade	10
1.5	The H-Mode	11
1.6	The I-Mode	12
1.7	Aim of this thesis	13
2	Heating Methods	15
2.1	Ohmic heating	15
2.2	Ion cyclotron resonance heating	15
3	Diagnostics in C-Mod	18
3.1	Thomson Scattering	18
3.2	Electron cyclotron emission	19
3.3	X-ray imaging crystal spectroscopy	19
4	Method of analysis: Power balance	21
4.1	Data preparation	23
4.1.1	Electron density	23
4.1.2	Electron temperature	24
4.1.3	Ion temperature	25
4.2	Diagnostic difficulties and constraints on the TRANSP calculations	27
4.3	The heat exchange term	29
5	Properties of the L-H transition	31
5.1	The L-H power threshold on ASDEX Upgrade	31
5.2	The L-H power threshold on Alcator C-Mod	35

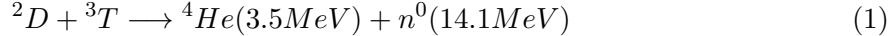
6	Analysis of the edge ion heat flux at the L-H transition	37
6.1	Time trace of several plasma quantities	37
6.2	Power deposition	39
6.3	Discussion of the heat exchange term	43
6.4	Error estimation	46
6.5	Q_i at the L-H transition	48
6.6	Influence of the different divertor configurations	49
6.7	Q_e at the L-H transition	53
6.8	Combining C-Mod and AUG results	54
6.9	Predictions for ITER	56
7	Summary and conclusion	57

1 Introduction

Today's energy production depends mostly on fossil fuels and fissionable nuclear material. Given that both of these sources are limited and getting more difficult to come by, a sustainable alternative is needed. Nuclear fusion is one of the most promising alternatives, because of almost unlimited fuel and a high energy gain. However, the attempts to construct a sustainable fusion reactor have not been successful yet.

1.1 Basic Principle of Nuclear Fusion

Nuclear fusion happens, when two light atomic nuclei come close enough to each other, for the strong force to take effect and form new particles. The products of these reactions are lighter than the original particles. This mass excess Δm is converted into kinetic energy of the fusion products according to $\Delta E = \Delta mc^2$. The preferred reaction for a fusion reactor is the deuterium-tritium reaction:



releasing 17.6MeV of kinetic energy. 2D , 3T and n^0 stand for deuterium, tritium and neutron. This reaction has the advantage of a very high fusion-cross-section at relatively low temperatures¹. Other possible fusion reactions are for example ${}^2D + {}^2D$, ${}^3T + {}^3T$ and ${}^2D + {}^3He$. The maximum of the ${}^2D + {}^3T$ cross-section σ lies at 64keV of relative kinetic energy which can be seen in figure 1 [1]. With the cross section we can describe the reaction parameter² $\langle\sigma v\rangle$ and with that the fusion reaction rate R_{DT} , i.e. the number of fusion reactions per unit of time and volume as

$$R_{DT} = n_D n_T \langle\sigma v\rangle \quad (2)$$

with the deuterium and tritium densities and relative particle velocity v [1].

¹Kinetic energy E of particles is directly proportional to their temperature T via $E = \frac{3}{2}k_b T$, wherein k_b is the Boltzmann constant. A 1eV particle has a temperature of 11600K, a 10keV particle therefore has a temperature of 116 million Kelvin. It is common in plasma physics to set the Boltzmann constant to 1, hence speaking of temperatures in units of energy (i.e. keV). This thesis will follow that convention.

²The reaction parameter $\langle\sigma v\rangle$ is the velocity space averaged cross section.

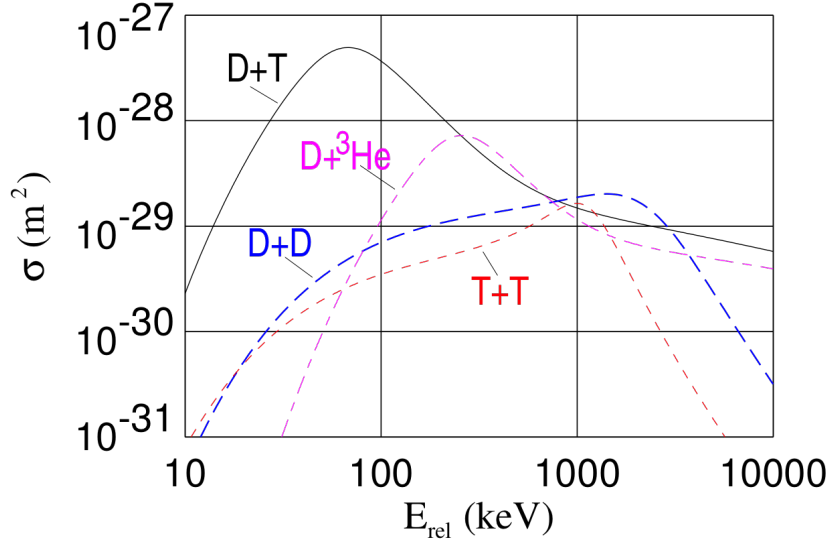


Figure 1: Fusion cross sections for DT , DD , TT and DHe^3 reactions depending on temperature. Figure adapted from [1]

However, since tritium is radioactive, most fusion experiments seldom have DT-campaigns and usually run with deuterium plasmas.

The problem with nuclear fusion is the electro-static force, which repels the positively charged particles. They must overcome the so called Coulomb wall for a fusion-reaction to happen.

Classically this requires very large energies, but a finite probability of reaction is obtained at lower energies thanks to the quantum tunneling effect. However, even with the tunneling effect, the nuclei still need a temperature of about 10keV for significant fusion reactions. At this temperature matter is in a fully ionized state called plasma.

The reaction parameter for the cross sections in figure 1 is shown in figure 2 and we can see, that at 10keV, the cross section itself is two orders of magnitude lower than the maximum, while the reaction parameter is reduced by only a factor of five.

But even at these temperatures the probability of a simple Coulomb collision is orders of magnitude higher than the probability for a fusion reaction. To ensure a significant number

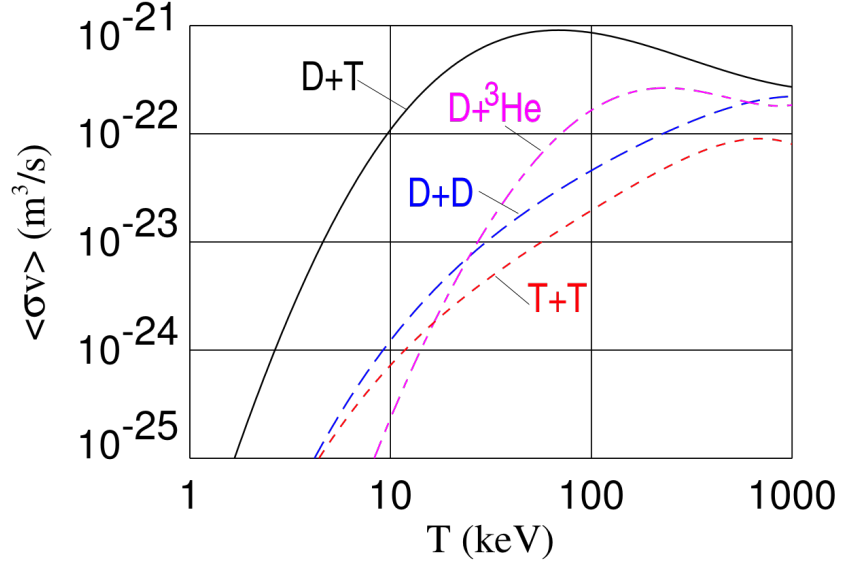


Figure 2: Reaction parameter for DT , DD , TT and DHe^3 reactions depending on temperature. Figure adapted from [1]

of fusion reactions, the particles need to be confined in order for them to participate in a sufficient amount of collisions. However, there is no material that could withstand 100 million Kelvin and if the plasma got in contact with the wall, it would almost instantly cool down, thus making fusion reactions impossible. The two main concepts for fusion devices are inertial confinement and magnetic confinement. This thesis will only address magnetic confinement since the data presented in it was acquired from ASDEX Upgrade and Alcator C-Mod, which are both tokamak machines (the tokamak design is discussed in section 1.2). Magnetic confinement uses the fact, that since a plasma consists of charged particles, it can be trapped inside a magnetic field.

1.1.1 Particle movement inside a magnetic field

Charged particles are subject to the Lorentz force $\vec{F}_L = q(\vec{E} + \vec{v} \times \vec{B})$ wherein q is the electrical charge of the particle, \vec{v} its velocity and \vec{E} and \vec{B} the background electric and magnetic field. Since there is no electric field in this example, the problem simplifies to $\vec{F}_L = q(\vec{v} \times \vec{B})$. To solve the equation of motion, the velocity is split in components

perpendicular and parallel to the magnetic field $\vec{v} = \vec{v}_\perp + \vec{v}_\parallel$. The parallel component is trivial, since $\vec{v}_\parallel \times \vec{B} = 0$ resulting in

$$m \frac{\partial \vec{v}_\parallel}{\partial t} = 0 \quad (3)$$

so all that is left is to solve is the perpendicular component

$$\frac{\partial \vec{v}_\perp}{\partial t} = \frac{q}{m} (\vec{v}_\perp \times \vec{B}) = \vec{\omega}_c \times \vec{r}_c \quad (4)$$

with the cyclotron frequency $\vec{\omega}_c = -\frac{q}{m} \vec{B}$ and the gyro-radius \vec{r}_c . m and q represent the particles mass and electric charge. We can see that a particle in a homogeneous magnetic field moves helically along the field lines with a gyration frequency $\vec{\omega}_c$.

1.1.2 Particle movement in crossed electric and magnetic fields

In this example a particle movement inside a magnetic field with a perpendicular electric field is examined. First, the velocity is again split in $\vec{v} = \vec{v}_\perp + \vec{v}_\parallel$ and the parallel component is again trivial

$$m \frac{\partial \vec{v}_\parallel}{\partial t} = q \vec{E}_\parallel \quad (5)$$

\vec{v}_\perp is more difficult because it is affected by both fields. To solve this problem the guiding center approach is used to split \vec{v}_\perp in $\vec{v}_\perp = \vec{v}'_\perp + \vec{v}_{E \times B}$ with

$$\vec{v}_{E \times B} = \frac{\vec{E} \times \vec{B}}{B^2} \quad (6)$$

With this approach the equation of motion for the perpendicular component simplifies to gyration around a guiding center

$$\frac{\partial \vec{v}'_\perp}{\partial t} = \frac{q}{m} (\vec{v}'_\perp \times \vec{B}) = \vec{\omega}_c \times \vec{r}_c \quad (7)$$

and a so called $E \times B$ -drift of the guiding center perpendicular to the electric and magnetic field (see figure 3).

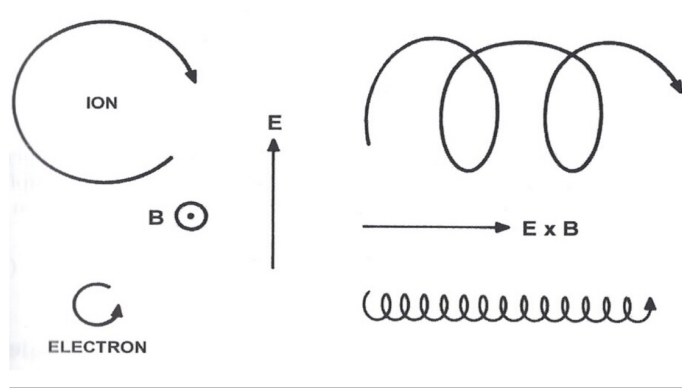


Figure 3: Illustration of the ExB-Drift. Figure adapted from [2].

This solution works for every force perpendicular to \vec{B} . Every force \vec{F} adds a drift velocity \vec{v}_F to the guiding centers motion according to

$$\vec{v}_F = \frac{\vec{F} \times \vec{B}}{qB^2} \quad (8)$$

Equation 8 shows, that in the case of a charge-dependent force, ions and electrons drift in the same direction, but charge-independent forces lead to a separation of positive and negative particles.

It is now clear, that plasma can be trapped by a magnetic field, because the particles follow the magnetic field lines. However, since we need to confine the plasma for a long time, linear devices such as the magnetic mirror are not suitable, due to high particle losses at the ends, which can be avoided by using a toroidal geometry. The most common toroidal design is the tokamak reactor.

It should be noted, that these short examples only look at a single particle and therefore ignore collisions, which play an essential role for plasma confinement.

1.2 The Tokamak

The 'toroidal chamber with magnetic coils', or short tokamak, is a Russian design for a thermonuclear fusion reactor. A tokamak traps fusion plasma in a doughnut shaped magnetic field. The toroidal field is created by several magnetic coils that are placed in a circle around the torus-axis, as can be seen in figure 4. The toroidal geometry results in two unfavorable drifts. Particles following the field lines are subject to the centrifugal

force and a force resulting from a gradient in the magnetic field. Both forces cause a drift according to equation 8 (the so called curvature drift and the ∇B drift) and result in a charge separation, leading to a vertical electric field. This electric field in turn leads to a radial $E \times B$ - drift which makes the plasma configuration unstable [3].

The tokamak design compensates these drifts by inducing a current into the plasma, adding a poloidal component to the magnetic field. The current is induced by using the plasma as a secondary coil of an oversized transformer. The resulting field is a toroidal field with a poloidal twist, i.e. helical field lines. The induced plasma current is also used for heating the plasma, which is discussed in section 2.1.

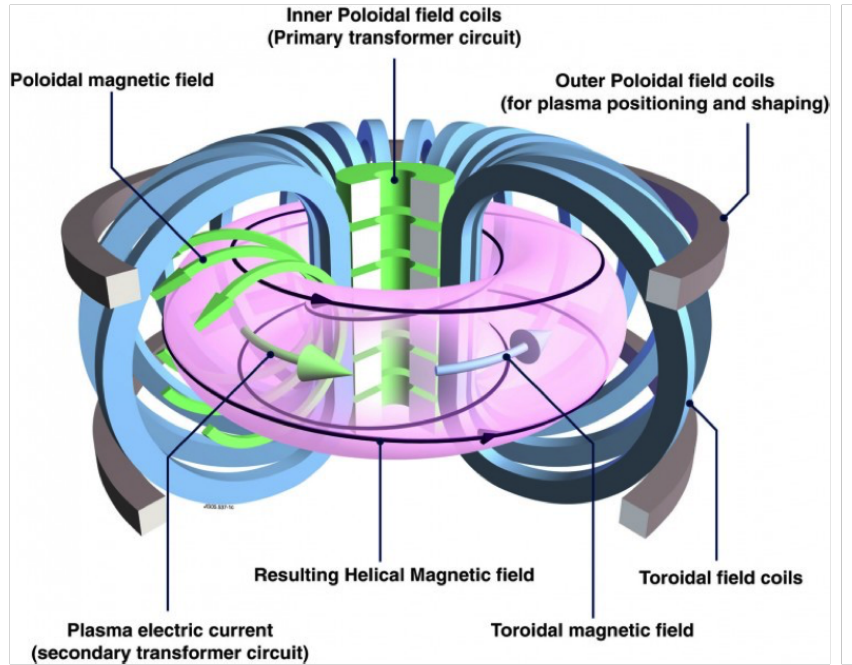


Figure 4: Schematic image of a tokamak configuration. The toroidal coils in blue create a toroidal field, illustrated by the blue arrow. The transformer in green induces a current in the plasma (green arrow in the plasma) which in turn creates a poloidal magnetic field illustrated by green arrows around the plasma. The resulting helical field line can be seen as a black line. Figure adapted from [4].

1.2.1 Flux surfaces and flux based coordinates

The magnetic field can be described with a vector potential $\vec{B} = \nabla \times \vec{A}$. Describing the tokamak with cylindrical coordinates (r, θ, z) allows to define a family of surfaces $\Psi(r, z) = rA_\theta = c$ with the c as a constant. One characteristic of these surfaces is that $\vec{B} \cdot \nabla \Psi = 0$ or in other words: the magnetic field lines define a set of so called flux surfaces and the plasma particles move along the field lines and consequently on these surfaces.

In an isotropic plasma in an equilibrium state, the momentum equation according to MHD is $\nabla p = \vec{j} \times \vec{B}$. This implies that the pressure gradient is perpendicular to the flux surfaces and that the plasma pressure is uniform on a flux surface.

Because particles move on the field lines, the transport coefficients for heat and particles along the flux surfaces is very high and it is reasonable to assume that temperature and density are also constant on a flux surface.

This motivates to describe density, temperature and pressure profiles as a function of normalized flux radius ρ which is 0 at the magnetic axis and 1 at the last closed flux surface. To get to a ρ like that, we must first introduce the toroidal and poloidal magnetic flux:

$$\Pi = \int_{A_{tor}} \vec{B} d\vec{A} \quad \Phi = \int_{A_{pol}} \vec{B} d\vec{A} \quad (9)$$

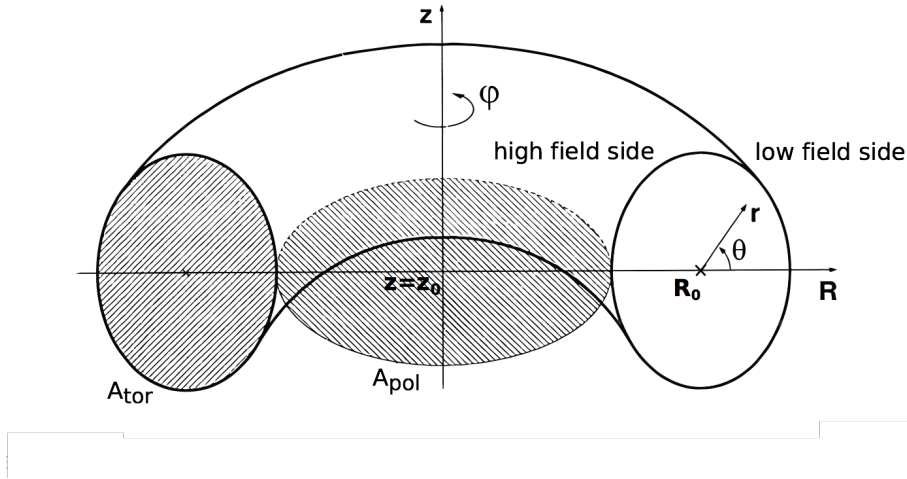


Figure 5: Illustration of A_{tor} and A_{pol} . Figure adapted from [5]

Π is the flux through A_{tor} and Φ the flux through A_{pol} , which are illustrated in figure 5. With two different fluxes we can define the normalized flux radii:

$$\rho_{tor} = \sqrt{\frac{\Pi - \Pi_a}{\Pi_s - \Pi_a}} \quad \rho_{pol} = \sqrt{\frac{\Phi - \Phi_a}{\Phi_s - \Phi_a}} \quad (10)$$

where the index a and s refer to the flux at the magnetic axis and the separatrix [5], respectively. Whether to use ρ_{tor} or ρ_{pol} usually depends on the problem at hand. In this thesis, ρ_{tor} is the only normalized flux radius used.

A high gain ($Q > 1$) fusion reactor (meaning that the reactor produces more energy, than is required to heat it to its operating temperature) has to fulfill the Lawson criterion [6], a triple product of the plasmas density, temperature and energy confinement time. Since the density in a tokamak is limited by the Greenwald density³ and the temperature is optimized for a maximum reaction rate, the key to achieving a sustainable reactor lies with optimizing the energy confinement time. Today, most tokamak reactors are only able to contain a fusion plasma for a couple of seconds and are therefore not able to produce

³The Greenwald density n_G is a density limit in tokamaks. Operating above n_G usually leads to disruptions. This is a tokamak specific problem since Stellarators are able to operate above the Greenwald density.

enough energy. The first reactor that is expected to surpass the Lawson criterion is ITER (**I**nternational **T**hermonuclear **E**xperimental **R**eactor or lat. 'iter': 'the way') currently under construction in France. The efficiency of a fusion reactor is expressed in the fusion power amplification factor Q , which is the ratio between power-output and power-input. $Q = 1$ is the so called break-even point and ITER is supposed to operate at $Q \geq 10$ [7]. Most of the research conducted in the field of nuclear fusion should benefit ITER by extrapolating the experimental results from smaller machines to make predictions about the reactor's behavior. The results presented in this thesis were acquired from ASDEX Upgrade (AUG) and Alcator C-Mod (short C-Mod).

1.3 Alcator C-Mod

Alcator C-Mod is a compact, high-magnetic field, diverted tokamak located at the MIT Plasma Science and Fusion Center in Cambridge, USA. The Alcator program was designed to explore the high field approach to fusion. With magnetic fields up to 8 Tesla, it can reach a plasma pressure and density higher than any other tokamak. C-Mod is the third machine in the Alcator series, following Alcator A and Alcator C. Alcator B was designed but never built because of a lack of funding. The operational phase in C-Mod started in 1993 and to this day C-Mod holds the record for highest plasma pressure in a magnetic confinement device. With regard to heating, C-Mod uses mainly radio frequency heating,

Major Radius	0.68m
Minor Radius	0.22m
Plasma Surface	$\sim 7\text{m}^2$
Max. Magnetic Field	8T
Plasma Current	0.4-2MA
Max. Pulse Time	4s
Heating Power	7MW
Plasma Temperature	over 80 Million Kelvin

Table 1: Parameters of Alcator C-Mod

in particular ICRH and lower-hybrid resonance heating. C-Mod is also equipped with numerous diagnostics, for example Thomson scattering diagnostics, X-ray imaging crystal spectroscopy, electron cyclotron emission, phase-contrast imaging, gas puff imaging, probe measurements, and active magnetohydrodynamic antennas. A complete summary of C-

Mod’s diagnostic capabilities can be found in [8]. On September 30th 2016, the last day of operation, C-Mod broke its own world record for plasma pressure in a tokamak machine (about 2 atmospheres).

1.4 ASDEX Upgrade

ASDEX Upgrade is a so-called mid-sized tokamak reactor located at the Max-Planck-Institut für Plasmaphysik (IPP) in Garching, Germany. It went into operation in 1991 following its predecessor ASDEX (‘**A**xial **S**ymmetrisches **D**ivertor **E**Xperiment’), which was the first experiment with a divertor instead of a limiter. AUG’s specific dimensions can be seen in Tab. 2. AUG is equipped with a variety of heating methods and diagnostics.

Major Radius	1.65m
Minor Radius	0.5m
Plasma Surface	$\sim 44\text{m}^2$
Max. Magnetic Field	3.9T
Plasma Current	0.4-1.6MA
Max. Pulse Time	10s
Heating Power	33MW
Plasma Temperature	over 100 Million Kelvin ($\sim 10\text{keV}$)

Table 2: Parameters of ASDEX Upgrade

The heating systems, besides the intrinsic ohmic heating, include radio frequency heating of electrons (ECRH) and ions (ICRH) as well as neutral beam injection (NBI). Although the maximum power of these heating systems add up to 33MW, only 24 have been experimentally realized [5], because using the full heating power requires a plasma density well above the usual AUG densities and due to experimental difficulties, these densities have not yet been reached. The diagnostics at AUG allow to measure electron density n_e , electron and ion temperatures (T_e and T_i) and several other quantities. The variety of diagnostics cannot be covered in this short section.

The issue with existing reactors is, that the energy cannot be confined long enough for sufficient fusion reactions to happen. This is a problem that ITER will hopefully overcome. By simply making the machine bigger, particles and heat have to travel a longer way from the plasma core to the plasma edge, which results in improved energy confine-

ment time and a higher probability for a fusion reaction to occur.

While ITER is supposed to surpass the break even point with its size, the idea behind high field tokamaks like C-Mod is to use very strong magnetic fields to improve plasma confinement. This would lead to much smaller and therefore much cheaper reactors. But the high temperature superconducting magnets that such a reactor would require are not yet available.

Another important aspect for improving the plasma confinement, was the discovery of the high-confinement mode (H-mode) at ASDEX in 1982, which can increase the energy confinement time by a factor of two [9].

1.5 The H-Mode

When the heating power in a tokamak surpasses a certain power threshold P_{L-H} , the plasma spontaneously enters a new state of improved confinement, the so-called H-mode [9]. In contrast to L-mode (low-confinement mode), plasmas in H-mode show improved energy-, particle- and impurity-confinement. It is widely accepted, that the improved confinement is a result of suppressed turbulent transport at the plasma edge, leading to the formation of a transport barrier [10]. This suppression results from a sheared $E \times B$ -flow at the plasma edge induced by a well in the radial electric field, E_r .

In H-Mode, density and temperature profiles develop the typical edge pedestal illustrated in figure 6. A consequence of the formation of the pedestals is the occurrence of edge localized modes (ELMs). The transport barrier leads to an increasing pedestal, resulting in steeper edge gradients. If the gradients become too steep, the pedestal collapses, leading to a violent burst of particles. These ELMs are magneto-hydrodynamic (MHD) instabilities, that are very straining for the reactor wall and the divertor.

The H-mode is the planned operational regime for ITER profiting from the high confinement time and using the quasi-periodical ELMs to remove impurities like helium-ash from the plasma.

The improved energy confinement in H-mode or any other plasma regime can be expressed by the confinement factor $H = \tau_E / \tau_E^L$, where τ_E is the energy confinement time and τ_E^L the confinement time in L-mode. For the H-mode, H is typically around 2 [3].

The economic importance of the H-mode is enormous. On one hand, τ_E increases approximately with R^2 , but on the other hand, costs increase with $\sim R^3$. This means that expenses increase much faster with machine size than the confinement time, making nu-

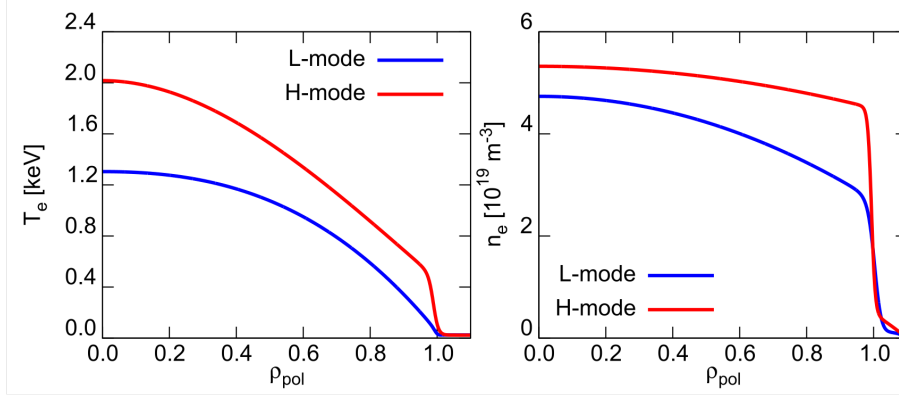


Figure 6: Illustration of the edge pedestal. Left the electron temperature profiles and right density profiles from AUG. The blue profiles show typical L-modes and the red profiles are typical for the H-mode. The edge pedestals can be clearly seen in both temperature and density. Figure adapted from [4].

clear fusion one of the most expensive research areas in modern physics. However, the costs of an ITER-like fusion reactor decrease with $\sim H^{-1.3}$ [11]. For $H=2$ that means a cost reduction of about 60%. Considering that ITER is costing billions of euros, it is clear, that without the H-mode, ITER would probably not have been funded.

1.6 The I-Mode

The intermediate mode or I-mode is another plasma regime of improved energy confinement. During early investigations at ASDEX Upgrade, the term ‘improved L-mode’ was used, but extensive studies at C-Mod coined the name I-mode.

A plasma in I-mode exhibits no increase in particle confinement relative to L-mode, yet the temperature profile develops an edge pedestal similar to H-mode [12]. The development of the pedestal indicates the formation of a heat transport barrier. This barrier can be attributed to turbulence reduction resulting from a steepening of E_r at the edge. While the E_r well is not as deep as during H-mode, it is clearly below the L-mode well [12]. To access the I-mode, a tokamak usually operates with unfavorable⁴ $B \times \nabla B$ configurations, and the heating power must overcome a power threshold $P_{L-I} < P_{L-H}$. The threshold for H-mode

⁴‘favorable’ and ‘unfavorable’ refer to a drift towards to or away from the X-point. The X-point is the point in figure 7 where the red flux surface crosses itself at the bottom of plasma, and at which the poloidal field goes to zero.

is usually two times higher under these conditions, than under favorable $B \times \nabla B$ configuration [13], which makes the access to I-mode easier. A plasma in I-mode can transition into H-mode, if enough power is provided.

The appeal of the I-mode lies in the H-mode like energy confinement, without the problem of impurity accumulation. Additionally the I-mode is ELM-free, which means less stress for the first wall and divertor components. However, P_{L-H} under favorable ∇B conditions is still lower than P_{L-I} under unfavorable conditions [12, 13], which is why ITER is envisioned with H-mode as standard regime, even though the I-mode could be a viable alternative.

1.7 Aim of this thesis

P_{L-H} in ITER is estimated to be about 50MW [14] and P_{L-I} is expected to be around 70MW [13]. These estimates are important for H- and I-mode access, since the envisioned heating power available for ITER will be 73MW, which is only slightly above P_{L-I} [15]. It is therefore essential to understand the physical mechanism behind L-H and L-I transitions. Previous research at ASDEX Upgrade has determined, that the edge ion heat flux $q_{i,edge}$ plays a crucial role for the access to H-mode [14, 15, 16]. An increase in $q_{i,edge}$ leads to a steeper ion temperature gradient ∇T_i and in turn to a steeper ion pressure gradient ∇p_i . According to the neoclassical transport theory, the radial electric field can be estimated with $E_r \approx \nabla p_i / (en_i)$ where e is the elementary charge, p_i the main ion pressure and n_i the ion density [16, 17]. It is well known, that the H-mode power threshold depends non-monotonically on line averaged plasma density. At a certain density $\bar{n}_{e,min}$, P_{L-H} has a minimal value, while any deviation from $\bar{n}_{e,min}$ leads to an increased power threshold. It is common to speak of a low and high density branch. Previous research in the low density branch [16] showed, that while the power threshold decreases with the density towards the minimum density, the surface integrated edge ion heat flux at the L-H transition $Q_{i,edge}^{L-H}$ increases linearly with density, scaling according to:

$$Q_{i,edge}^{L-H,fit} = 0.18\bar{n}_e \quad (11)$$

wherein $Q_{i,edge}^{L-H,fit}$ is in MW and \bar{n}_e the line-averaged density in 10^{19}m^{-3} . The aim of this thesis is to seek a similar dependency in C-Mod discharges, and to determine whether the ion heat flux is indeed the driving parameter for a L-H transition, and not an AUG-specific property. For the investigation of the L-H and L-I transitions, selected discharges from

Alcator C-Mod will be analyzed. The heat flux can be calculated via time dependent power analysis using the code TRANSP [18]. To determine the ion heat flux from the core to the edge, one must first calculate the heat flux in the ion and electron channel separately and then the heat exchange between the two species. The full-wave TORIC code [19] is implemented in TRANSP and is used to calculate ICRH heating.

Then, similar to [16], the ion heat flux should be calculated for L-H and L-I transitions at different densities, to determine its impact on them.

Section 2 of this thesis will discuss the used heating methods, and section 3 the diagnostics. The method to calculate the ion heat flux as well as data preparation for TRANSP is presented in section 4. An introduction of previous research on L-H transitions at AUG and C-Mod can be found in section 5. And finally, in section 6 and 7, the final results are presented and discussed.

2 Heating Methods

Tokamaks usually have a variety of different heating methods available. The most basic one comes from the intrinsic heating of the plasma current. This so-called Ohmic heating can heat a plasma up to 1keV [3]. To reach higher temperatures, additional heating systems such as neutral beam injection and radio frequency heating are needed. Radio frequency heating uses electro-magnetic waves to resonantly excite the gyrating plasma species. There are two common heating schemes: the ion cyclotron resonance heating (ICRH) and the electron cyclotron resonance heating (ECRH) [3]. This chapter will only discuss Ohmic and ICRH since all C-Mod discharges presented in this thesis only use these two methods.

2.1 Ohmic heating

The tokamak design provides an intrinsic ohmic heating due to the toroidal plasma current that is required for an equilibrium state. The ohmic heating results from the plasmas resistivity caused by collisions of its particles. The power density is given by [3]

$$P_{\Omega} = \eta j^2 \quad (12)$$

where η is the plasma resistivity and j the current density. This heating method is limited by η , which is not constant, but decreases with $T^{-3/2}$. The hotter the plasma, the more ineffective is the ohmic heating, which is why additional auxiliary heating is needed in tokamak devices.

2.2 Ion cyclotron resonance heating

The ICRH scheme is based on the resonant absorption of electro-magnetic waves in a magnetized plasma. To be absorbed, the wave needs to fulfill the resonance condition [3] for the angular frequency

$$\omega - k_{\parallel} v_{\parallel} - n\omega_{ci} = 0 \quad (13)$$

wherein ω is the angular frequency, $\omega_{ci} = |\vec{\omega}_{ci}| = \frac{qB}{m}$ the ion cyclotron frequency and n a positive integer. If $n = 1$ the wave is called fundamental wave and for $n > 1$ they are referred to as higher harmonics of the fundamental wave. The Doppler shift is expressed in $k_{\parallel} v_{\parallel}$, with the wave number k_{\parallel} and particle velocity v_{\parallel} parallel to the magnetic field. ICRH

frequencies typically lie between 30 and 120 MHz [3]. The magnetic field in a tokamak decreases as R^{-1} [5] and with it ω_{ci} . This means, that there is only a small radial region, where the resonance condition is fulfilled for a given frequency. Thus the power deposition can be controlled by adjusting either the magnetic field or the wave's frequency.

The only wave that can propagate through the magnetic field in the MHz frequency range is the compressional Alfvén wave (fast magneto-sonic wave). The refractive index for propagation perpendicular to the magnetic field can be derived from the dispersion relation of the cold plasma model [5] and yields

$$\tilde{n}_{\perp}^2 = \frac{\left[\sum_j \frac{\omega_{pj}^2}{\omega_{cj}(\omega + \omega_{cj})} - \tilde{n}_{\parallel}^2 \right] \left[\sum_j \frac{\omega_{pj}^2}{\omega_{cj}(\omega - \omega_{cj})} + \tilde{n}_{\parallel}^2 \right]}{\left[\sum_j \frac{\omega_{pj}^2}{(\omega^2 - \omega_{cj}^2)} + \tilde{n}_{\parallel}^2 \right]} \quad (14)$$

wherein j is the species index and ω_{pj} the plasma frequency for each species. If the refractive index becomes zero, the wave can no longer propagate through the plasma. This is commonly referred to as *cut off*. Equation 14 gives a cut off condition (i.e. $\tilde{n}_{\perp}^2 > 0$)

$$\sum_j \frac{\omega_{pj}^2}{\omega_{cj}(\omega + \omega_{cj})} > \tilde{n}_{\parallel}^2 \quad (15)$$

A region where this is not the case is a so called *evanescent layer*. The cut off condition depends on the electron density, such that evanescent layers occur if the density becomes too low [3]. That poses the obvious problem of an evanescent layer between the antenna and the plasma. It is possible for the wave to tunnel into the plasma, but that requires the antenna to be very close to the plasma surface for efficient coupling.

Theoretically, the best mode for heating gyrating ions in a deuterium plasma would be the left-circular polarized fundamental mode E_+ . The circular polarization is not fixed by the antenna, but rather by the interaction of the wave and the plasma. At the fundamental mode, the wave is purely right-circular E_- in the resonant region and cannot be absorbed [5, 20]. Experiments with second harmonic ICRH at TFR⁵ have shown a remarkably good absorption [21]. This effect was later explained by residual hydrogen in the deuterium plasma, which was resonant at the fundamental frequency since it has twice the q/m

⁵Tokamak de Fontenay-aux-Roses

ratio of deuterium. This heating scheme is called *minority heating* [3] and is common in most fusion machines. For efficient minority heating, the minority concentration should be $< 5\%$, since the absorption rate decreases rapidly for higher concentrations [5]. For ITER however, the hydrogen minority heating scheme will not work, since the α -particles from fusion reactions have half the q/m of hydrogen and would absorb the ICRH efficiently [5]. Since heating the high-energy fusion alphas must be avoided, ITER will operate with a ${}^3\text{He}$ minority scheme.

ICRH primarily increases the perpendicular velocity component of hydrogen particles in the high energy tail of the hydrogen distribution function and it is common to speak of a perpendicular and parallel temperature, T_\perp and T_\parallel . In other words, the ICRH forces hydrogen to gyrate faster and faster around the field lines. The hot particles then transfer their kinetic energy via collisions to the plasma bulk particles. Above a critical energy E_{crit} the ions predominantly heat the electrons, and below E_{crit} transfer power to the bulk ions. The critical energy is given by [3]

$$E_{crit} = 14.8T_e \left[\frac{A_m^{3/2}}{n_e} \sum_j n_j \frac{Z_j^2}{A_j} \right]^{2/3} \quad (16)$$

where A_m is the atomic number of the minority and T_e the electron temperature. The summation is made over all other plasma species with A_j and Z_j being the atomic and the charge number and n_j the density. Choosing a distinct minority concentration, can therefore allow to heat either electrons or ions. However, in an experimental setup, choosing the concentration is a very difficult task.

3 Diagnostics in C-Mod

As a research tokamak, C-Mod is equipped with a wide variety of diagnostics. A comprehensive summary of them can be found in [8]. This chapter will give a short overview of the methods to measure ion and electron temperature as well as electron density, since these are the quantities that are most important for the heat flux calculations with TRANSP.

3.1 Thomson Scattering

Thomson scattering (TS) is a widespread method to measure electron temperature and density. Being a non-perturbing diagnostic, it is used at most hot plasma experiments to gather information about the electron distribution function [22]. Powerful pulsed lasers penetrate the plasma, and the beam photons scatter from free electrons. Since the electrons in the plasma are always in motion, the spectrum of the detected photons exhibits Doppler broadening characteristic of the electron velocity distribution. Therefore electron temperature and density can be measured by examining the width and height of the photon spectrum. To use Thomson scattering the photon energy must fulfill the condition $\hbar\omega \ll mc^2$, where mc^2 is the scattering particles mass times the speed of light squared [22]. Additionally, it is important that the wavelength of the photons is small compared to the Debye length of the plasma [23].

The experimental implementation of TS is rather difficult. Since the photons get scattered in every direction and the detector has a limited view, only a small fraction of the scattered photons actually reach the detector. This obviously poses a significant problem for the signal to noise ratio and getting decent signals requires a lot of work to minimize potential noise [22]. The TS system implemented on C-Mod uses two Nd:YAG lasers at 50Hz with a spatial resolution of 1-2cm in the core

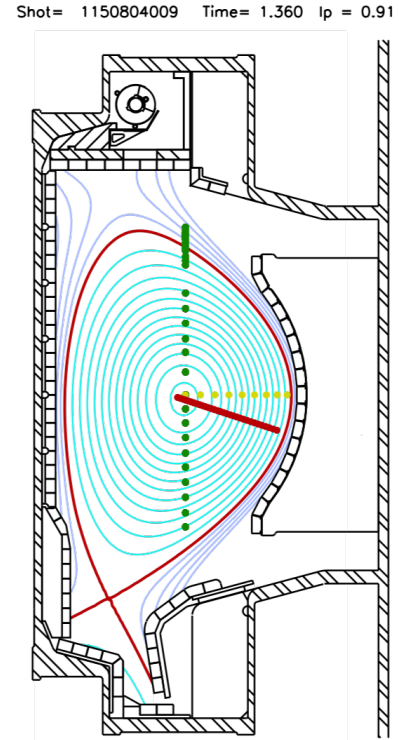


Figure 7: Poloidal view of C-Mod, showing field lines (blue), separatrix (red), closed magnetic flux surfaces inside the plasma (turquoise), view-points of TS (green points), GPC/GPC2 (yellow points) and FRC (red points).

and 1-2mm at the plasma edge [24, 25]. This improved spatial resolution at the edge is illustrated in figure 7. The green points in this figure symbolize the view-points of the TS.

3.2 Electron cyclotron emission

Electron cyclotron emission is a diagnostic to measure electron temperature and is used in most tokamaks. The electrons' gyro-motion around the field lines causes them to emit electromagnetic waves. Detectors in C-Mod use the second harmonic extraordinary (X) mode emission with frequencies up to 500 GHz [8] to measure the spectrally resolved absolute wave intensity $I(\nu)$. The frequency ν relates to the cyclotron frequency $\nu = \omega_c/2\pi$ and depends on the magnetic field. So just like RF heating can be deposited in a fixed radial region by adjusting the frequency, because of $B \propto 1/R$, the emitted frequency determines a radial region of origin [4]. The intensity follows Planck's law for black body radiation:

$$I = \frac{\omega_c^2}{8\pi^3 c^3} k_B T_e \quad (17)$$

and provides information about the electron temperature [4]. Additionally a Maxwellian electron velocity distribution and an optical thick plasma have to be assumed and relativistic and Doppler shifts in frequency are neglected [4].

The ECE data in this thesis was measured by two grating polychromators GPC and GPC2. GPC has nine, and GPC2 nineteen spatial channels. The viewpoints can be seen in figure 7. ECE in general provides very robust measurements at a high time resolution.

3.3 X-ray imaging crystal spectroscopy

The ion temperature profiles used for this thesis were acquired by x-ray imaging crystal spectroscopy (XICS) using a high resolution x-ray spectrometer with spatial resolution (HIREXSR). HIREXSR is a passive diagnostic, that measures X-ray line radiation from medium Z impurity ions (in this case argon) in the plasma with a time resolution of about 20ms [26].

The hydrogen- or helium-like argon gets distributed through the plasma and continuously collides with other plasma particles. These collisions excite the remaining bound electrons and by relaxation into lower orbits, they emit line radiation. The radiation from each line of sight is reflected from a set of two crystals, creating a spectrum for each line of sight. The

peaks in these spectra are widened by the Doppler broadening of the moving argon ions. Since we assume, that the argon and the main ions are in a state of thermal equilibrium, the Doppler broadening gives us information about the ion temperature. To get from one spectrum per line of sight to a flux-surface based spatial profile, we have to assume poloidal and axial symmetry, and that temperature can be described as a function of ρ_{tor} . The HIREXSR analysis code THACO can then invert the data into an ion temperature profile [26]. Figure 8 illustrates the process of creating ion temperature profiles.

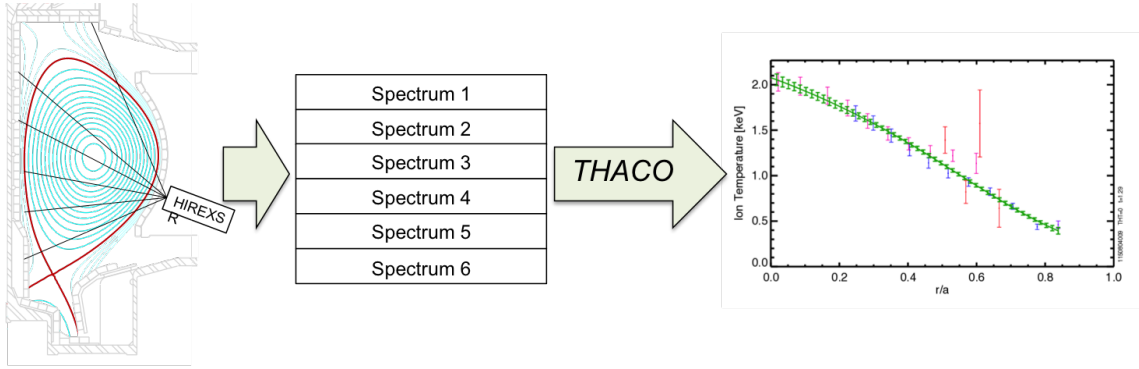


Figure 8: Schematic outline of the T_i profile preparation. The detector with the two crystal collects the spectra for each line of sight and THACO then inverts them into temperature profiles. Note, that the detector position and the lines of sight are just an illustration and do not represent the actual detector configuration.

While the HIREXSR data provides good profiles for the core, its spatial resolution at the edge is poor. C-Mod is, however, equipped with charge exchange recombination spectroscopy (CXRS). This diagnostic measures radiation from impurities at the edge and allows to measure the ion temperature at the edge. If CXRS data is available, combining it with HIREXSR data would lead to more accurate profiles, which would be beneficial to future TRANSP calculations.

4 Method of analysis: Power balance

The idea behind the heat flux calculation is that in a power equilibrium the amount of heating power that flows into the plasma (minus the losses) is equal to the total heat flux, that transports heat radially up to the plasma surface. In other words, the heating power minus the radiated power is equal to the surface integrated heat flux. The surface integrated heat flux can again be split up into the amount of heat that is transported by the electron channel and by the ion channel. The respective power balance to determine them is:

$$Q_e = P_{ohm} + P_{aux,e} - Q_{ie} - P_{rad} \quad (18)$$

$$Q_i = P_{aux,i} + Q_{ie} \quad (19)$$

with P_{ohm} as the ohmic power, that only heats electrons, $P_{aux,e}$ and $P_{aux,i}$ the auxiliary heating of the electron and ion channel, P_{rad} the radiated power (calculated from the emissivity profile determined from foil bolometers [27]) and Q_{ie} the volume-integrated electron-ion heat exchange. This term is therefore added to the ion channel and deducted from the electron channel. It is particularly important for this analysis and will be discussed in detail later in this chapter. The use of capital letters in equation 18 and 19 means, that they represent the respective quantity at a given radius, integrated from the plasma core to said radius. For example, if q_{ie} is the amount of heat exchanged in a volume element at a given time (so in W/cm^3) then Q_{ie} , at a given radius, is the sum of q_{ie} from all volume elements inside of that radius.

The time dependent power balance analysis was performed using the transport code TRANSP. In general, every species s in a plasma can be described with the distribution function $f_s(\vec{x}, \vec{v})$ and from it the equations for particle, motion and energy conservation can be derived. The kinetic equation is:

$$\frac{\partial f_s}{\partial t} + \vec{v} \cdot \nabla f_s + \frac{q_{c,s}}{m_s} (\vec{E} + \vec{v} \times \vec{B}) \cdot \nabla_v f_s = \left(\frac{\delta f_s}{\delta t} \right)_{coll} \quad (20)$$

wherein \vec{v} is the particle velocity, $q_{c,s}$ the particle charge and m_s the particle mass. Inte-

grating this equation over the velocity space as well as multiplying it with $m_s \vec{v}$ and $m_s v^2/2$ and then integrating over the velocity space gives the equations for particle, momentum and energy conservation:

$$\frac{\partial n_s}{\partial t} + \nabla \cdot (n_s \vec{u}) = S_s \quad (21)$$

$$m_s n_s \frac{D \vec{u}_s}{Dt} = n_s \langle \vec{F}_s \rangle - \nabla p_s - \nabla \cdot \overleftrightarrow{\pi}_s + \vec{R}_s \quad (22)$$

$$\frac{3}{2} \frac{\partial p_s}{\partial t} + \nabla \cdot \left(\frac{3}{2} p_s \vec{u}_s \right) + p_s (\nabla \cdot \vec{u}_s) (\overleftrightarrow{\pi}_s \cdot \nabla) \vec{u}_s + \nabla \cdot \vec{q}_s = Q \quad (23)$$

with $\vec{u}_s = \langle \vec{v} \rangle_s$, $\langle \vec{F}_s \rangle = q_{c,s} (\vec{E} + \vec{u}_s \times \vec{B})$, $\frac{D}{Dt} = \frac{\partial}{\partial t} + (\vec{u}_s \cdot \nabla)$, pressure p_s , viscosity tensor $\overleftrightarrow{\pi}_s$, a collision term R_s , heat flux q_s and source terms for particles and heat S_s and Q [28].

TRANSP solves the energy balance equation for local transport coefficients χ_s as a function of space and time [28]. Therefore it requires several parameters, some of which can be measured, and the rest need to be modeled by TRANSP. Density, temperature and current are treated as functions of flux surface and time, and toroidal symmetry is assumed. This simplifies the geometry to one flux based radial component. The respective heat fluxes can then be described as:

$$q_s = n_s \chi_s \nabla T_s \quad (24)$$

To calculate the ICRF depositions into ions and electrons TRANSP uses the implemented full-wave code TORIC [19]. The most important measured quantities for these calculations are T_e (TS and ECE), T_i (HIREXSR) and n_e (TS).

4.1 Data preparation

TRANSP is not able to use raw data directly from the diagnostics. The data first needs to be fitted and then loaded with loading routines, which take the fitted data and interpolate it to the required grid. Electron temperature and density profiles were fitted with polynomial fits using the PSFCs fiTS software [29], and the fits for the ion temperature profiles came from THACO [26]. fiTS and THACO are both written in IDL. To ensure that the fits were reasonable, the profiles up to 100 ms before the transition were checked individually for outliers or other issues with the measurement, which could hinder the fitting routines.

For the electron density and temperature this is straight forward and, aside from being very time consuming, checking the profiles was not a big problem. The T_i profiles on the other hand proved to be very difficult. Since HIREXSR does not collect radial profiles but rather a spectrum for each line of sight, and THACO relies on statistical routines to invert the raw data into temperature profiles, getting the right profile requires expertise and experience.

4.1.1 Electron density

The electron density was measured with TS and fitted with fiTS. Figure 9 shows a typical n_e profile. The core TS (green) and edge TS (blue) were fitted individually (light blue and yellow curve) and then combined to one fit (black). The two vertical dashed lines illustrate the merge area, where core and edge fit are joined together. The dotted dashed line marks the magnetic axis. There is a typical outlier in the edge TS as well as four points that lie clearly above the other data points. They do have enormous error bars and do not seem to affect the fit badly. The outlier is crossed out, because it was removed manually. In every manually checked profile outliers like these were excluded from the fit and if necessary, the merging area broadened and moved to better fit the data. Note, that in the core, the fit consists of the core fit and in the edge, of the edge fit. Because of that, the edge fit can only be seen in the core, and the core fit only in the edge and the actual fit can only diverge from them in the merging area.

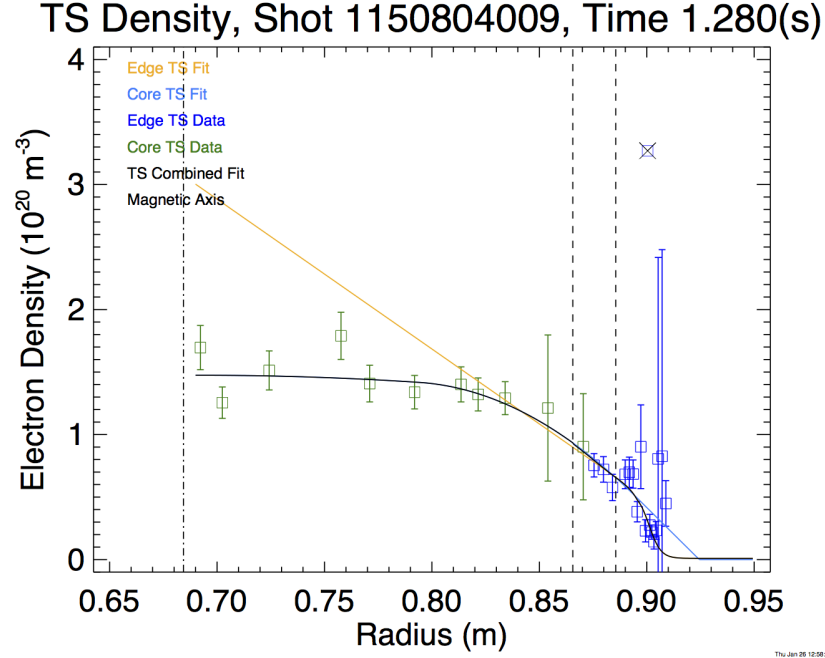


Figure 9: Density profile from fiTS. Core TS (green squares), edge TS (blue squares), core fit (light blue line), edge fit (yellow line) and combined fit (black line).

4.1.2 Electron temperature

The electron temperature was also fitted with fiTS, but unlike density, T_e is measured by both ECE and TS. This led to far more data points in figure 10. The fitting procedure was similar to the one used for density. Outliers, like the one at $R = 0.765$ were excluded and the merging area adjusted. At the edge, the temperature was measured by TS only. The reason for that is that the plasma edge is no longer optically thick, which is why the ECE measurements are not reliable in that region.

fiTS stores density and temperature profiles for each shot in one IDL file together.

Temperature, Shot 1150804009, Time 1.280(s)

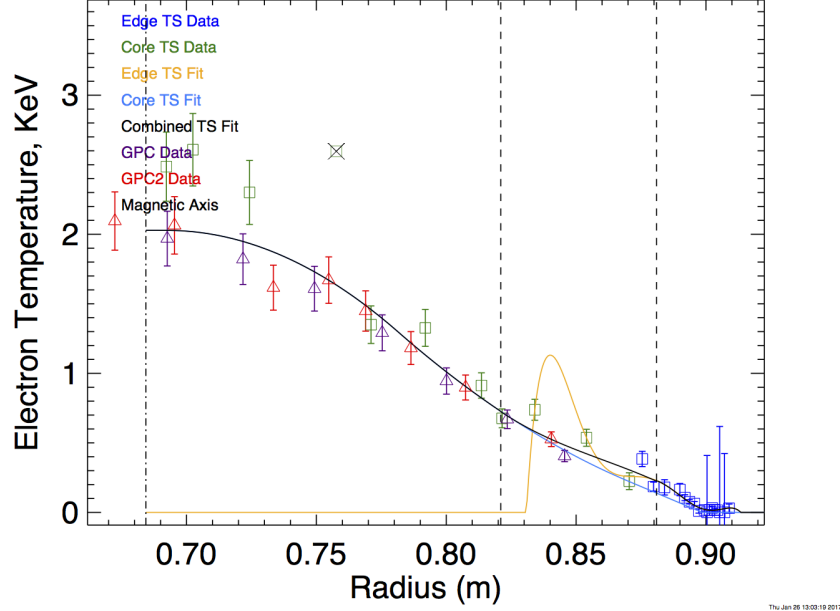


Figure 10: Electron temperature profile from TS (core: green, edge: blue), ECE (GPC: purple, GPC2: red), core fit (light blue line), edge fit (yellow line) and combined fit (black line).

4.1.3 Ion temperature

The assembly of the ion temperature profiles proved to be the most time-consuming part of the analysis. The inverted T_i profiles from the MDSplus tree can be displayed with the HIREXSR.TIFIT from THACO. Figure 11 shows a T_i fit from a typical discharge. There are four different sets of data points with different colors: Branch B inverted in purple, Branch A inverted in blue, Branch B line average in red and Branch A line average in lilac. Branch A and B refers to the detector configuration to detect line radiation from helium and hydrogen like argon. The 'Branch A(B) inverted' data is the actual inverted data from THACO. However, if a line of sight only intercepts a few flux surfaces at the edge, the average temperature from the line spectrum is a reasonable estimate for the temperature on these surfaces. So the inverted data describes the core temperature well, and the line

averaged data improves the fit at the edge.

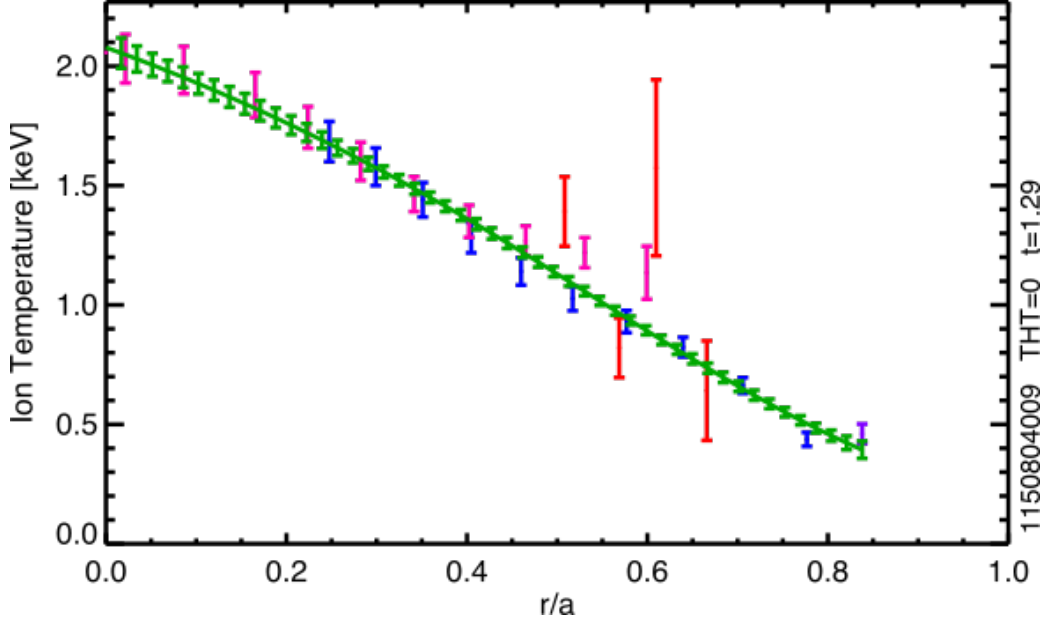


Figure 11: Ion temperature profile from THACO: Branch B inverted (purple), Branch A inverted (blue), Branch B line average (red), Branch A line average (lilac) and the fit in green.

In the core, argon is mostly in a hydrogen like configuration which is why there are no points from Branch A in the core of figure 11. When a discharge is loaded with THACO, it automatically chooses the radial region where the data points (purple, blue, red and lilac) are included in the fit. For example in figure 11, only the purple Branch B inverted points between r/a equals 0 and 0.65 are in the plot and are included in the fit. On the other hand Branch A average points are only included in a very narrow region at the edge, so there is only one lilac point in figure 11.

It is however possible, to include for example Branch A line average points in a wider region. In figure 11, the lilac point of Branch A line average is included around $r/a = 0.85$, but it is possible to include points that are closer to the edge into the fit. Doing that can have a drastic effect on the shape of the fit and one has to keep in mind that HIREXSR is not very reliable at the plasma edge.

Just like the T_e and n_e profiles, the T_i profiles were checked manually for outliers. However, THACO does not allow the exclusion of single points like fITS so the only possibility

to exclude them is by changing the radial region of the whole set, usually leading to the loss of more points than just the outlier. It was sometimes better to just accept the small negative effect of an outlier, than taking out too many points. For example, in figure 11 there is a clear outlier in red at $r/a = 0.6$, however, its effect on the fit is not visible, and to exclude it, other data points that agree very well with the rest of the data would have to be excluded as well. In general, the regions were only altered if too many outliers clearly distorted the fit in a non-physical way. The difficulty to exclude outliers in T_i is one of the main error sources for this thesis.

Another reason, why the T_i profiles were so difficult to obtain was, that on some run days data Branch B was not available, which led to less accurate profiles, which could lead to miscalculations in TRANSP.

4.2 Diagnostic difficulties and constraints on the TRANSP calculations

With pretransp, the collected data can be prepared for TRANSP and sent to PPPL in Princeton. It also allows the user to pose some constraints on the calculation.

One important aspect for the calculation of ICRF power deposition into the plasma is the hydrogen minority concentration. The measurement of minority concentration is made with a simple spectrometer looking at the plasma edge. Figure 12 shows a time trace of $H/(H + D)$ from an example discharge. H and D represent the measured densities of hydrogen and deuterium. This definition does not take impurity concentrations into account which typically are at 1-2% level.

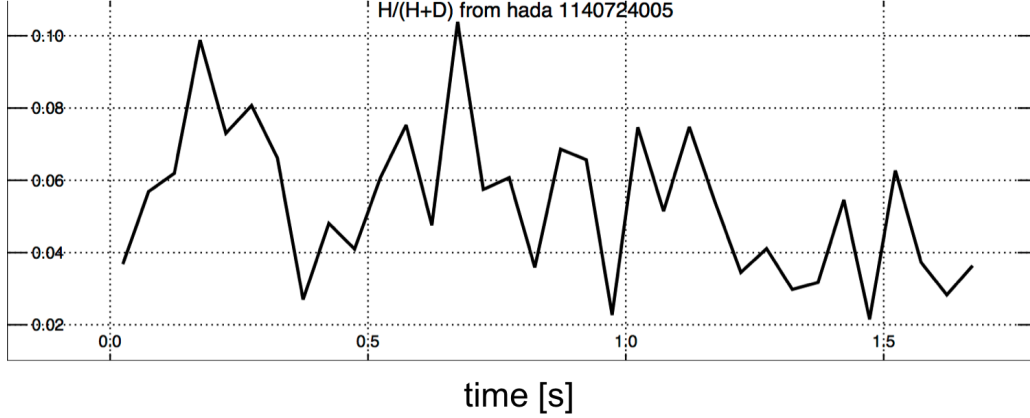


Figure 12: Hydrogen concentration.

Since the measurement has significant uncertainty and statistical variations, the hydrogen concentration was constrained to 5% in all calculations, which is a reasonable estimate for C-Mod plasmas.

Unlike the minority concentrations, the Z_{eff} measurements do not tend to be very noisy, but suffer from a systematic uncertainty. Z_{eff} was constrained to a fixed value, which was close to the average measured Z_{eff} just before the transition. However, the influence of Z_{eff} on the heat flux calculation is negligible.

The uncertainty that impacted the calculations the most, was posed in the ion temperature. HIREXSR does not provide good edge data, but because of the high collisionality in C-Mod it can be argued, that at the outer regions of the plasma $T_e = T_i$. The edge T_e from TS and the edge T_i from charge exchange spectroscopy agreed very well, which is why T_i was constrained to be equal to T_e outside of $\rho_{\text{tor}} = 0.9$. Figure 13 shows the temperature profiles that were used in one TRANSP run. At the edge, the T_i profile jumps up to the T_e profile, illustrating the effect of the temperature constraints. Of course this shape is unrealistic, but since the measurements from high density discharges in C-Mod are at the limit of the diagnostic possibilities, some constraints were necessary and their effect on the final results are bearable due to the low densities outside of $\rho_{\text{tor}} = 0.9$.

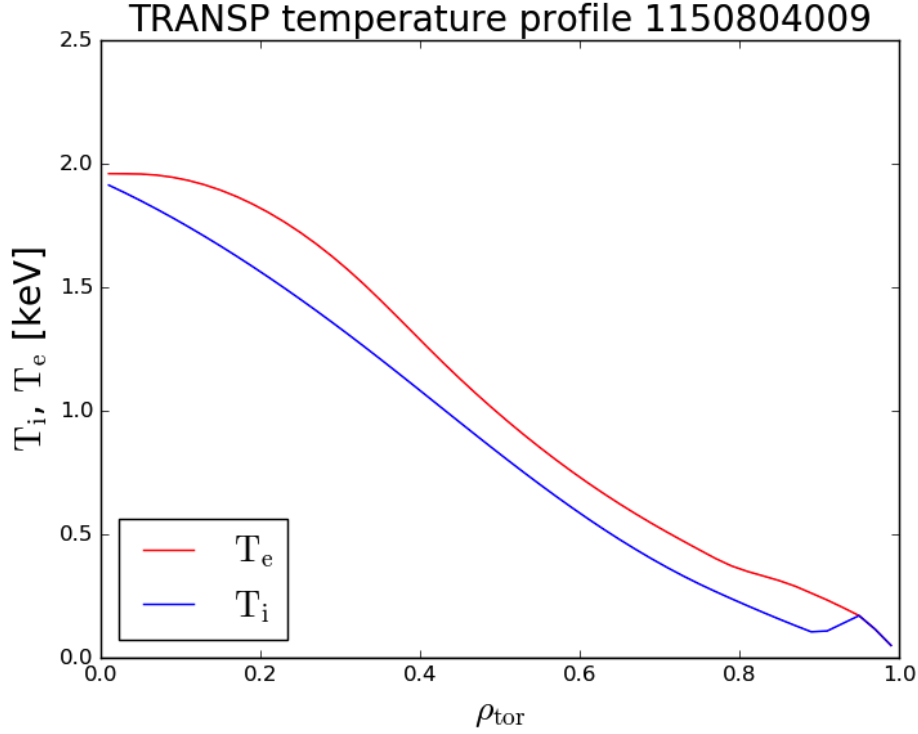


Figure 13: Temperature profile from TRANSP, ion temperature in blue and electron temperature in red.

4.3 The heat exchange term

The reason why constraints on the temperature profiles have a large effect on the heat flux calculations is that, since the ICRF power is mostly deposited in the core, any changes in the ion heat flux outside of the deposition area stem from the heat exchange term. The heat exchange term reads

$$q_{ie} \propto n_e n_i \frac{T_e - T_i}{T_e^{3/2}} \quad (25)$$

and leads to a couple of issues:

- Because C-Mod is a high density tokamak, the exchange term is especially prominent due to $n_e n_i$.

- The high density also leads to a stronger coupling of electrons and ions. Because of that, the difference of T_e and T_i is very hard to determine correctly. AUG is equipped with an ECRH system and is therefore able to deposit the entire heating power in the electron channel. The ion heat flux then only consists of the exchange term and because the electron temperature is much higher than the ion temperature the $T_e - T_i$ term is easy to measure and due to $T_e^{-3/2}$ the exchange term gets smaller.
- The density dependence can also explain the U-shaped power threshold. Because of the weaker heat exchange in the low density branch, more power is needed to reach the critical ion heat flux (see section 5.1).
- Similar to the density dependence of q_{ie} , the $T_e^{-3/2}$ term leads to a weaker heat exchange at high electron temperatures. Which explains, why more auxiliary heating power is needed to access H-mode with only ECRH.
- The $T_i = T_e$ constraint at the edge in TRANSP consequentially sets the heat exchange to zero at the outermost radii.

So the main problem with the heat exchange term in C-Mod was the strong coupling of electrons and ions due to high densities, which makes it hard to determine the temperature difference. Sometimes the difference was so small, that the fitted T_i profile was above the T_e profile. Fits like that are possible if, for example, the error bars of both measurements overlap. If the T_i fit is above the T_e fit in only a very narrow radial region, the calculations were useless. In cases like those, the heat exchange term becomes negative, meaning that heat flows away from the ions and into the electrons. In extreme cases, that led to a negative edge ion heat flux, especially in the high density regions, where all calculations lead to strange results. This is why every shot, that had $T_i > T_e$ fits before the transitions was excluded from the dataset.

One way to improve future calculations is to include edge ion temperature measurements from charge exchange spectroscopy into the T_i profiles.

5 Properties of the L-H transition

The heating power is defined as $P_{loss} = P_{tot} - dW/dt = P_{OH} + P_{aux} - dW/dt$. In this definition, P_{OH} is the intrinsic Ohmic heating, P_{aux} the auxiliary heating and dW/dt the change in energy stored in the plasma. Losses due to radiation are usually not subtracted in power threshold studies [14]. As mentioned in section 1.5, the heating power must overcome P_{L-H} to access H-mode. The power threshold depends on several parameters, such as density, magnetic geometry, favorable or unfavorable particle drift. Multi-machine studies led to an empirical scaling law for P_{L-H} in [MW] for tokamaks with standard magnetic confinement and favorable ion ∇B drift

$$P_{L-H,scal} = 0.049 \bar{n}_e^{0.72} B_T^{0.8} S^{0.94} \quad (26)$$

with the line average density $\bar{n}_e [10^{20} m^{-3}]$, the toroidal magnetic field $B_T [T]$ and the plasma surface area $S [m^2]$ [30]. However, it is well known that there are significant deviations from that scaling law. Instead of an almost linear dependence on \bar{n}_e , the power threshold exhibits a non-monotonic 'U-shaped' behavior.

5.1 The L-H power threshold on ASDEX Upgrade

The power threshold for ASDEX Upgrade has been the subject of several investigations over the years and has been found to depend on a variety of parameters. AUG is usually operated with D-plasmas but early experiments with H as well as ^4He have shown, that P_{L-H} increases by a factor 1.8 in H-plasmas, and 1.4 in ^4He -plasmas [14]. In these experiments, the high density branch was very well described by $P_{L-H,scal}$. Between 2003 and 2007 the inner carbon wall was gradually replaced by a tungsten wall. The 2008 campaign was the first with only tungsten-coated plasma-facing components. The new wall led to a P_{L-H} reduction by 25% [15] as can be seen in figure 14. Additionally, D and ^4He plasmas have shown no noticeable difference in threshold power since the 2008 campaign. Figure 14 also shows, that P_{L-H} does not depend on the auxiliary heating method and exhibits the non-monotonic 'U-shape'. Results from [15] also showed that $\bar{n}_{e,min}$ and P_{L-H} decrease with the plasma current.

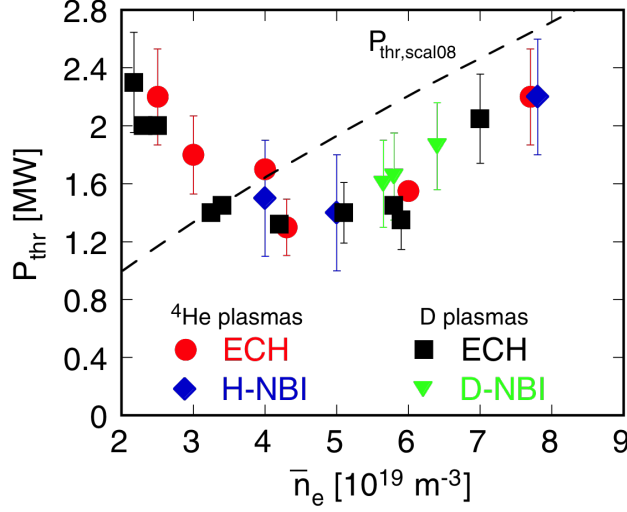


Figure 14: AUG results for the power threshold versus line-integrated density for ^4He and D plasmas with the full tungsten wall. ECH refers to electron cyclotron heating and H-NBI and D-NBI are neutral beam heating with hydrogen and deuterium. Note that P_{thr} is used for the threshold power instead of P_{L-H} . $P_{thr,scal08}$ refers to equation 26 and it can be seen that the power threshold with the tungsten wall is below the scaling. Figure adapted from [15]

3D magnetic field perturbations are used to mitigate ELMs in tokamaks. These mitigations are necessary for ITER since the violent heat and particle burst of a large ELM could severely damage the machine. Results from [31] indicate that these perturbations lead to an increased P_{L-H} .

[15] recognized the importance of the ion channel for L-H transitions. The paradigm, that the H-mode transport barrier is a consequence of reduced turbulent transport due to sheared $E \times B$ flows at the plasma edge, is widely accepted. The sheared flows are caused by ∇E_r at the radial electric field well at the plasma edge. E_r is caused by the main ions, according to the neoclassical estimate $E_r \approx \nabla p_i / (en_i)$ [16, 17]. An increase in heating power would in turn lead to an increased ion heat flux $q_{i,edge}$. The increased edge ion heat flux would cause a higher edge ion temperature gradient ∇T_i and since $n_i T_i = p_i$, this would lead to an increased ∇p_i . It should be noted, that this line of reasoning is valid because n_i does not change significantly just before the L-H transitions [15].

The increased $q_{i,edge}$ could lead to self-induced zonal flows (ZFs) and geodesic acoustic

modes (GAMs) which can trigger the transition. However, without a background E_r well, the H-mode cannot be maintained since ZFs and GAMs disappear after the transition [15]. The role of $q_{i,edge}$ has been further studied in [32] by conducting experiments with sole ECRH, NBI and NBI with ECRH. For the shots with ECRH only, the entire input power went into the electron channel, so that the ion heating resulted from electron-ion collisions. The collisional energy exchange q_{ie} is $\propto n_e n_i (T_e - T_i) / T_e^{3/2}$ [32].

In the ECRH experiments, P_{L-H} , while still 'U-shaped', exhibited a strong dependence on I_p . In figure 15 the power threshold versus density from 1MA and 0.6MA shots is presented. P_{L-H} for 0.6MA shots is clearly lower than with 1MA current. This can be attributed to $T_e^{-3/2}$ in q_{ie} . With higher current, the electron temperature is higher leading to a reduction in energy exchange between ions and electrons which is why more power is needed to reach the necessary $q_{i,edge}$ [32]. Contrary to the difference in P_{L-H} , figure 15 shows that $Q_{i,edge}^{L-H}$ still follows the scaling law in equation 11 within the error bars. It should be noted that the surface integrated ion heat flux Q_i is used here for the sake of convenience, since it is also measured in MW making it directly comparable to P_{L-H} .

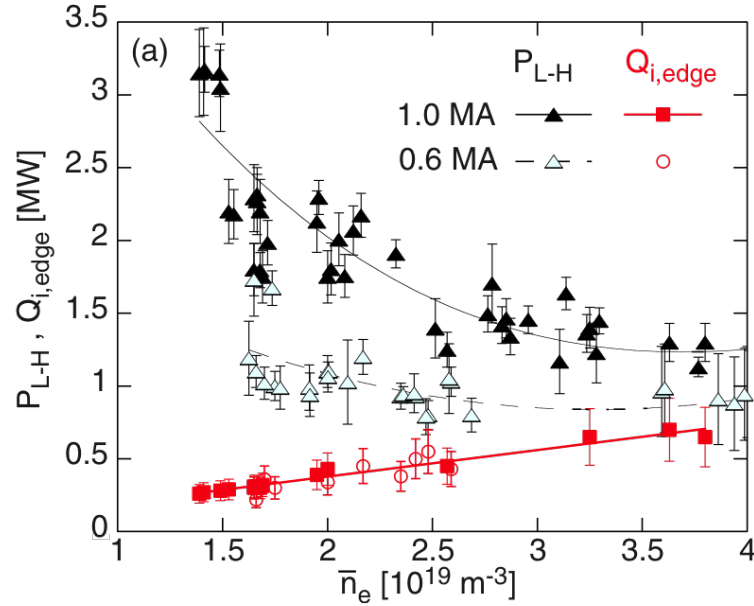


Figure 15: Power threshold and surface integrated ion heat flux versus density for 1MA and 0.6 MA. The graph clearly shows a I_p dependance of P_{L-H} but $Q_{i,edge}^{L-H}$ shows no current dependance. Figure adapted from [32]

With NBI heating (configured so that about 50% of the beam heats the ions directly) the threshold power is about 40% lower than with ECRH, underlining once again the importance of the ion channel. In the experiments with NBI and ECRH combined (ECRH less than 700kW) P_{L-H} increased at least by the ECRH power and could reach the values with only ECRH. $Q_{i,edge}^{L-H}$ did not depend on the ECRH power, however, with NBI (with and without ECRH) $Q_{i,edge}^{L-H}$ was slightly above the prediction of equation 11 [32].

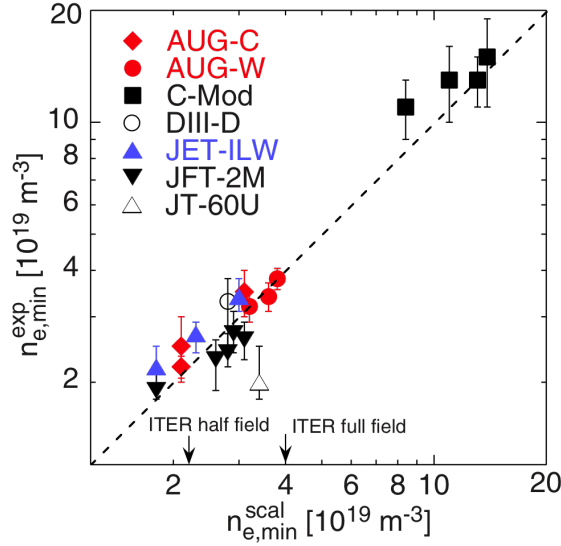


Figure 16: Minimal density from different tokamaks versus minimal density as predicted by the scaling law. AUG-C and AUG-W refer to ASDEX Upgrade with carbon and tungsten wall and JET-ILW refers to JET with the ITER-like wall. The minimal density from JT-60U significantly deviate from the scaling law. It is surprising that the law also predicts $n_{e,min}$ for C-Mod so well. Figure adapted from [32].

Additionally to the observations of the ion heat flux, [32] also explained the minimal density for the L-H transition as an effect of the electron-ion coupling. This idea leads to a scaling law to predict $n_{e,min}$ for different tokamaks that yields

$$n_{e,min}^{scal} = 0.7 I_p^{0.34} B_T^{0.62} a^{-0.95} (R/a)^{0.4} \quad (27)$$

[32]. a and R refer to the plasma's minor and major radius. This scaling law predicts

$n_{e,min}$ very well as can be seen in figure 16. Surprisingly, the scaling law that was found at AUG very accurately describes $n_{e,min}$ for C-Mod, which is a high field, compact tokamak that operates in a much higher density region than all the other machines.

5.2 The L-H power threshold on Alcator C-Mod

An empirical study of L-H transitions at C-Mod showed, that P_{L-H} can be influenced by several parameters but the overall shape exhibits the same 'U-shape' as P_{L-H} in other machines [33].

Since C-Mod only uses RF-heating as auxiliary power, the net power simplifies to $P_{net} = P_{OH} + cP_{RF} - dW/dt$ with c being the percentage of RF power absorbed by the plasma, which is set to one for simplicity in [33]. In figure 17a) the threshold power is plotted over the line-averaged density at 5.4T. The ITER-scaling represented by the almost linear line clearly does not represent the data as well as the dashed line that was fitted to the data. It only describes the data in a narrow density region slightly above the minimal density. It is better described by $P_{L-H} = 1.5/\bar{n}_e^2 + 0.2\bar{n}_e^{3.5}$ [33]. Figure 17b) shows a similar plot with a different magnetic field.

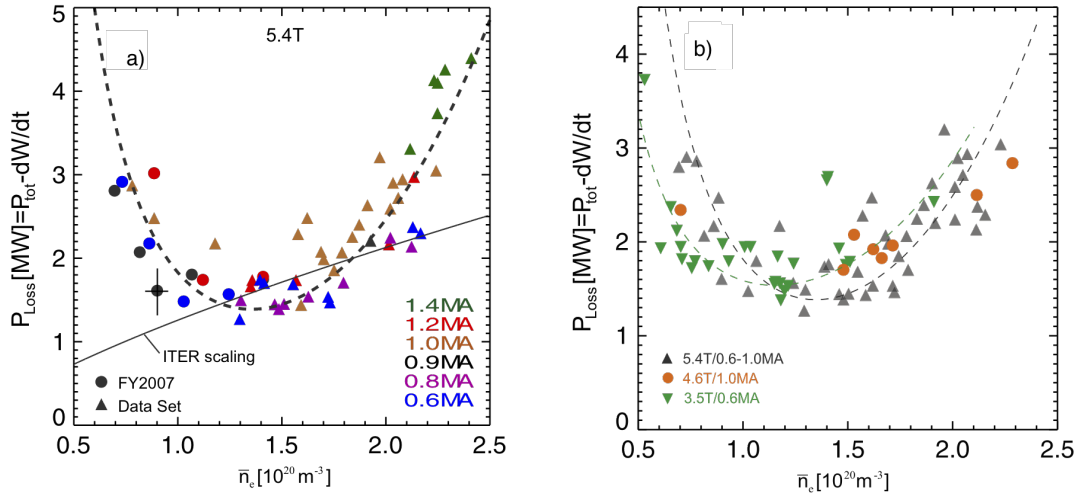


Figure 17: L-H power threshold over line-averaged density. a) shows P_{L-H} with different plasma currents and $B_T = 5.4$. b) shows the power threshold over density with different toroidal field strength. The grey triangles represent the data from a), the orange circles and the green triangles show the power threshold with 4.6T and 3.5T. Figure adapted from [33].

While $\bar{n}_{e,min}$ changes with the strength of the magnetic field, the 'U-shape' remains. The green dashed line is fitted to the 3.5T data points with the same method that was used to fit the dashed line in figure 17a). It shows, that the minimum density varies with the magnetic field strength.

A different study showed an inverse correlation between the power threshold and the distance between X-point and the outer divertor strike point (outer divertor leg length or OLL) [34]. By switching from a vertical plate divertor configuration to a slot divertor, the OLL increased by approximately 50-100% which led to a P_{L-H} reduction by a factor of ≈ 2 .

While the paradigm that the H-mode transport barrier is a consequence of reduced turbulent transport due to sheared $E \times B$ flows at the plasma edge is widely accepted, the underlying physics behind the L-H-transition have been under investigation for the past years and are still not definitively clarified. The H-mode can be accessed, regardless of the used auxiliary heating method [10], but recent studies have shown the main ions to play a major role for the transition [14, 15, 16].

6 Analysis of the edge ion heat flux at the L-H transition

The data set presented in this thesis was collected from selected discharges from the 2014, 2015 and 2016 C-Mod campaigns. Density, ion and electron temperature profiles as well as several other quantities were collected and used to calculate the ion heat flux at the plasma edge using TRANSP as described in earlier sections. All plots in this chapter, except figure 18 and 30, show TRANSP output.

6.1 Time trace of several plasma quantities

Figure 18 shows a typical discharge from the data set. The top two boxes show the plasma current and magnetic field, which are constant for the duration of the shot. Because of the steady current, the ohmic power remains more or less constant, in L-mode prior to 1.28s. The auxiliary ICRF power is increased in three power-steps from zero, to 0.3, to 0.5, to 0.7 MW. Shortly after the last step, the plasma transitions into H-mode at about 1.28s. The transition time is commonly defined by a drop in the $D\alpha$ -signal (bottom Box). In this discharge, the $D\alpha$ -drop is not that sharp and abrupt, which is not typical for a L-H transition, but it is still visible. Immediately after the transition, density and edge temperature start to increase, due to the formation of the edge transport barrier. The H-mode is highlighted by the blue shaded area, and ends shortly after the ICRF power is turned off.

Every C-Mod discharge has a unique number, that reads 1-year-month-day-xxx, where xxx counts the discharges of that particular day. So for example discharge number 1140801002 stands for the second discharge from the first of August, 2014. The numbers of the discharges presented in this section can be found in table 3. This table also contains the respective line average density, surface integrated edge ion and electron heat flux, the threshold power and the time of transition from L-Mode into H-Mode.

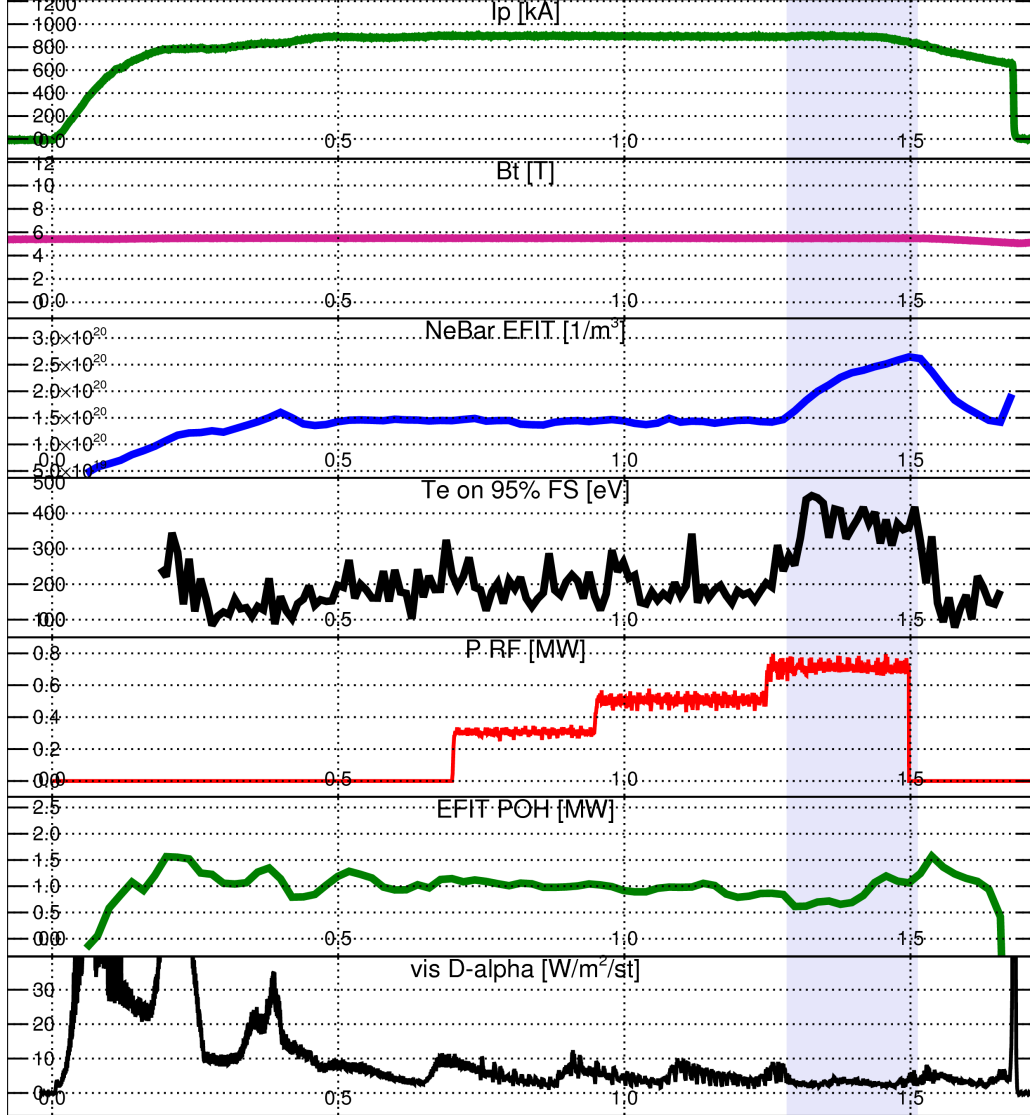


Figure 18: Time traces of selected quantities, for discharge 1140724005. From top to bottom: plasma current, magnetic field, line-average density, edge electron temperature from TS, auxiliary RF power, ohmic power, visible $D\alpha$ - emission. The shaded area marks the time in which the plasma is in H-mode.

Discharge number	$n_e[10^{20}m^{-3}]$	$Q_i[MW]$	$Q_e[MW]$	$P_{L-H}[MW]$	t_{L-H}
1150804009	1.362	0.992	0.639	1.754	1.29
1150804010	1.220	0.621	0.555	1.329	0.7
1150804021	0.943	0.572	1.410	2.207	1.23
1150804026	1.080	0.837	1.005	1.899	1.27
1140724005	1.467	0.956	0.662	1.920	1.28
1140724006	1.439	1.105	0.532	1.837	1.01
1140801002	1.495	0.860	0.657	1.826	0.74
1140801003	1.107	0.391	1.171	1.874	0.72
1140801004	1.227	0.668	1.367	2.079	1.11
1140801005	1.040	0.762	1.290	2.175	1.12
1140801007	0.971	0.576	1.064	1.931	1.18
1140801009	1.424	0.898	1.288	2.201	1.34
1140801012	1.302	0.821	1.254	2.305	1.21
1140801013	1.240	0.975	1.219	2.406	1.12
1140801018	1.462	0.990	0.793	1.114	1.29
1140801021	1.272	0.658	0.877	1.747	0.72
1140801026	1.080	0.598	0.230	2.050	1.26
1140801030	0.992	0.646	0.906	1.622	0.61
1140801032	1.066	0.491	1.860	2.753	1.18

Table 3: Discharge numbers with density, surface integrated ion and electron heat flux at $\rho_{tor} = 0.98$, heating power (just prior to the L-H transition) and transition time.

6.2 Power deposition

The surface integrated edge ion heat flux is not a standard TRANSP output, but it does calculate the power deposition into the electron and ion channel, as well as the heat exchange. To calculate Q_i , the ICRH power into the ion channel ' $p_{i,ich}$ ' and the heat exchange term ' q_{ie} ' are added, multiplied with the respective volume element and integrated over radius. This is illustrated in figure 26.

Figure 19 shows the radial profiles of the ICRH power deposition into the ion and electron channel, as well as the heat exchange term. Most of the power is deposited in the electron channel inside of $\rho_{tor} = 0.4$, which is in agreement with section 2.2, since the power is deposited only in a small radial region. This also means that the ion heating depends significantly on the electron ion heat exchange.

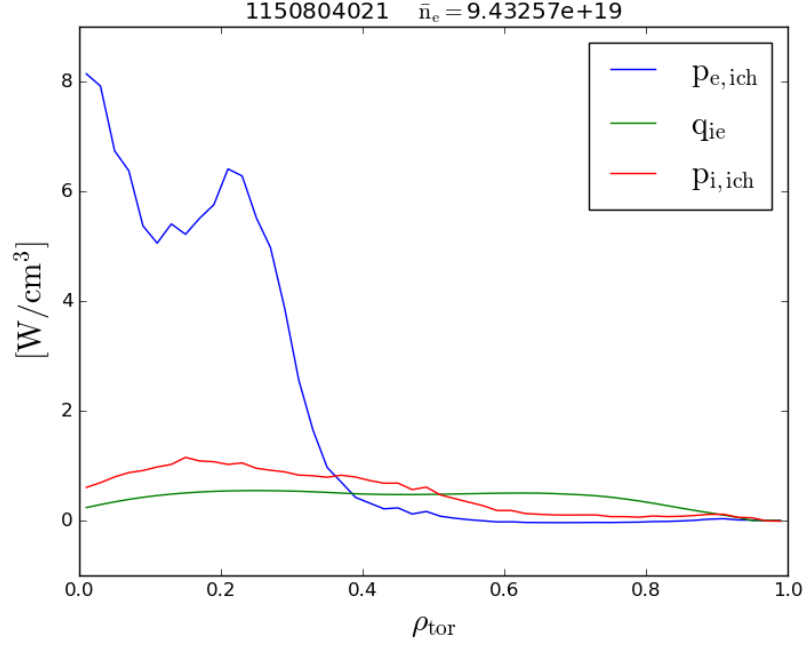


Figure 19: ICRF power deposition into the ions (red), electrons (blue) and the heat exchange term (green).

By integrating the $p_{i,ich}$ and q_{ie} profiles from figure 19, and adding the two we get the profile surface integrated ion heat flux as can be seen in figure 26. This profile can be interpreted as the power flowing outwards through the respective flux surface. To further study the importance of the individual terms of the heat flux, we will examine two discharges, one with low and one with rather high density:

Discharge number	$\bar{n}_e[10^{20}m^{-3}]$	$Q_i[MW]$	$P_{L-H}[MW]$	t_{L-H}
1150804021	0.943	0.572	2.207	1.23
1150804009	1.362	0.992	1.754	1.29

Table 4: Example discharges.

Figure 20 shows the density profiles for these two discharges, 1150804021 in blue and 1150804009 in green. Note, that the slight bump at $\rho = 0.8$ in the higher density profile is not the start of the edge pedestal, but rather an artifact from the merging of the core and edge fit in fiTS.

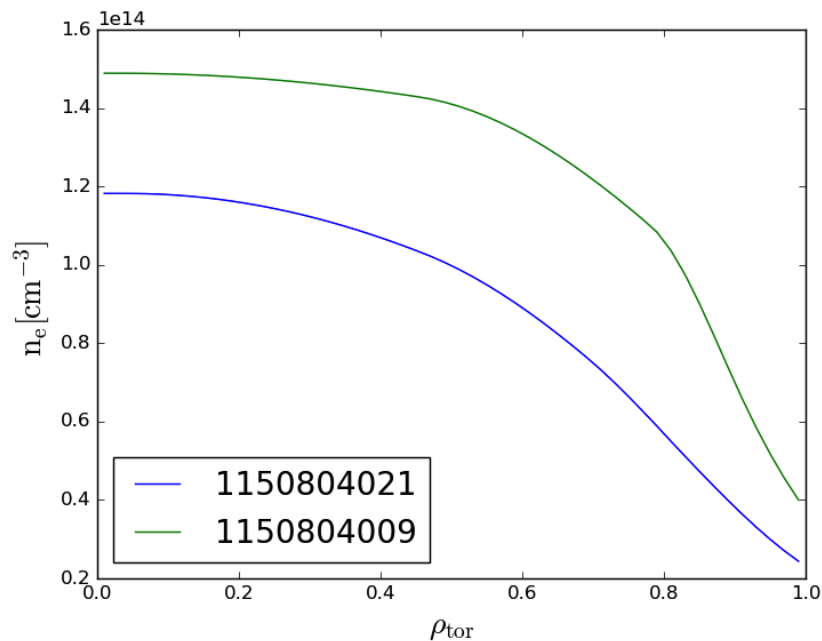


Figure 20: Density profiles of example discharges 1150804021 and 1150804009.

Figure 21 compares the ICRF depositions into the ion channel for the two discharges. In both cases, most of the power is deposited in the plasma core. The deposition is given in $[Wcm^{-3}]$, so multiplied with the respective volume element and integrated over radius, as mentioned above, we obtain a profile that shows how much of the ICRF power flows outwards at any given ρ_{tor} . These profiles are shown in figure 22 and while overall more ICRF power is deposited in the higher density discharge, we will see that the difference will be augmented by the heat exchange term.

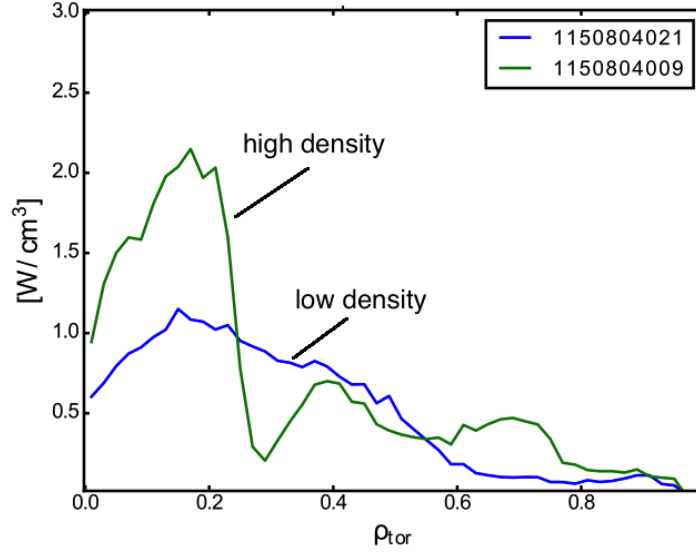


Figure 21: ICRF power deposition in the ion channel for 1150804021 (blue) and 1150804009 (green) shortly before the L-H transition.

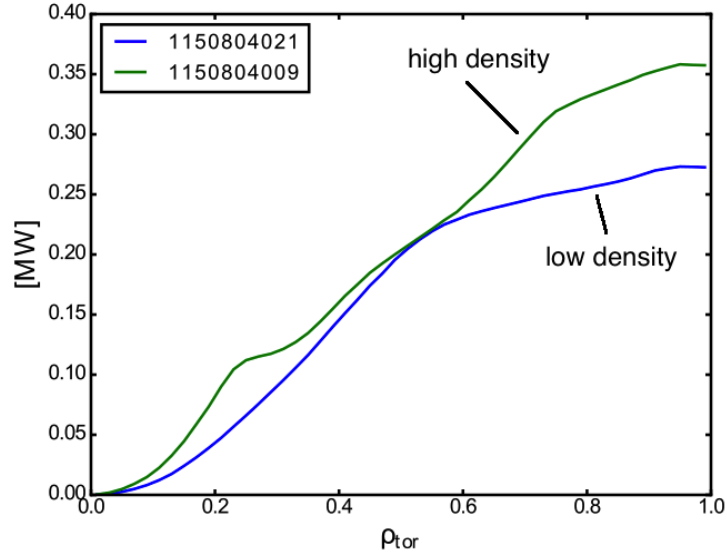


Figure 22: Profiles of the surface integrated ICRF power deposition in the ion channel for 1150804021 (blue) and 1150804009 (green) shortly before the L-H transition.

6.3 Discussion of the heat exchange term

The heat exchange term plays a major role for the ion heat flux, because the entire ohmic power and most of the auxiliary power go right into the electron channel (see figure 19). Therefore, a substantial part of the ion heat flux stems from the exchange between ions and electrons.

Since the goal of this thesis is to investigate the relation between $Q_{i,edge}$ and \bar{n}_e , the density term $n_e n_i$ in equation 25 is of immense importance. Figure 23 shows the profiles of the heat exchange just before the transitions for the low and high density example discharges. Note, that closer to the edge, the heat exchange profiles decrease because of the decreasing density, however, their jumps to zero are due to the $T_i = T_e$ constraint in TRANSP.

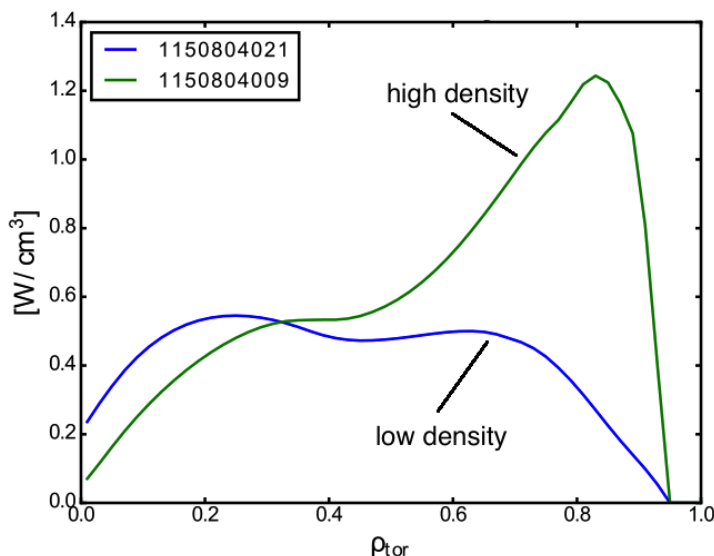


Figure 23: Profiles of ion-electron heat exchange for a low (blue) and high (green) density discharge just before the L-H transition.

Figure 24 shows the surface integrated heat exchange similar to figure 22. Two features are striking:

First, we can see the immense importance of the density term $n_e n_i$ because the heat exchange of high density discharge is about a factor 2 higher and also approximately a factor two higher than the ICRF power into the ion channel for both discharges. Secondly, al-

though the low density discharge deposits more power per cubic centimeter in the core in figure 23, the surface integrated heat exchange is not that different in the core. This can be explained with the very small plasma volume in the core.

The $T_i = T_e$ constraint leads to flattening of the surface integrated heat exchange because it is zero close to the edge. This is more prominent for the high density discharge.

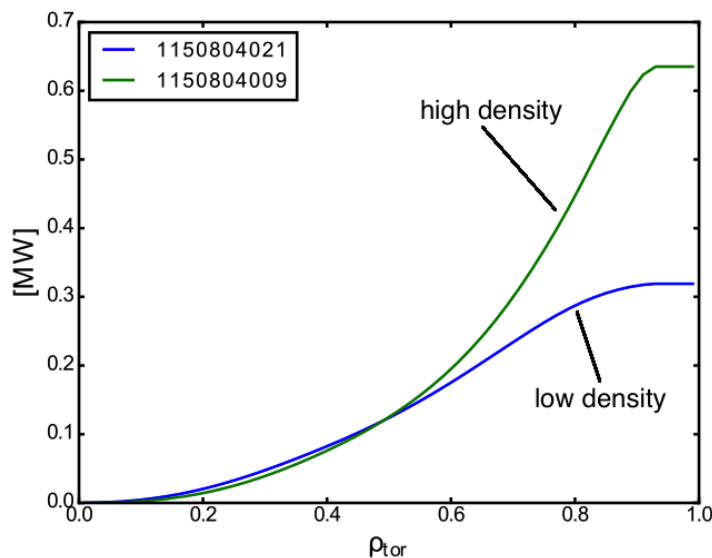


Figure 24: Surface integrated heat exchange profiles for 1150804021 (blue) and 1150804009 (green) shortly before the L-H transition.

For the sake of completeness, figure 25 shows the electron and ion temperature profiles for both discharges. Due to the lower density in 1150804021, the coupling between electrons and ions is weaker, which also results in a more distinct difference in temperature. 1150804009 on the other hand shows T_i and T_e very close to each other. At higher densities, it becomes increasingly challenging to separate the two temperature profiles and because of the $T_e - T_i$ term, this analysis does not make sense for discharges with a much higher density.

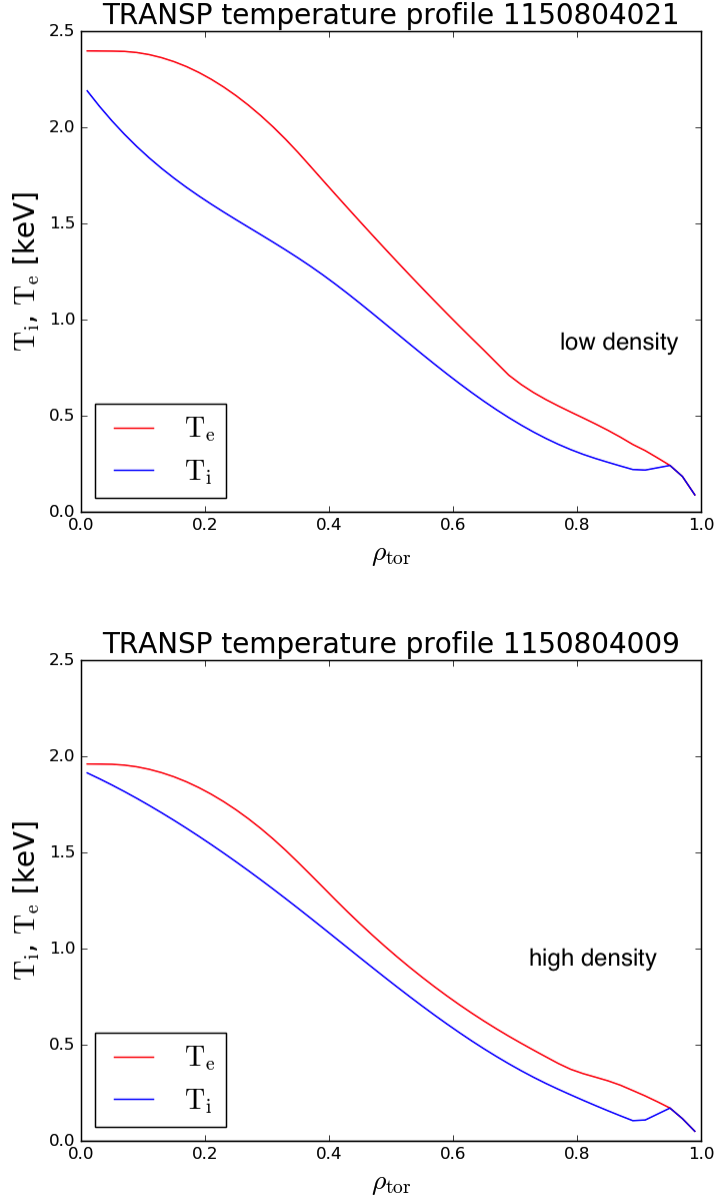


Figure 25: Electron and ion temperature profiles in red and blue at the L-H transition for discharge number 1150804021 and 1150804009.

In the end, we obtain the surface integrated ion heat flux by adding the power from the ICRF and the heat exchange term. Figure 26 shows this for the two example discharges

and illustrates once again the importance of the heat exchange term. In the core, the ICRF portion is dominant, but closer to the edge, Q_{ie} becomes ever more prominent.

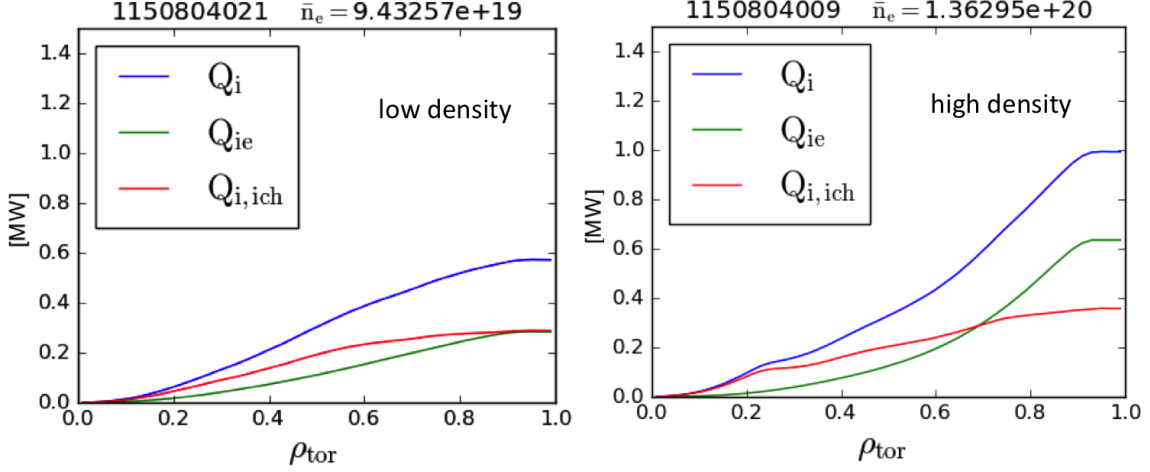


Figure 26: Profiles of the surface integrated heat flux, as well as its components at the L-H transition for discharge number 1150804021 and 1150804009.

6.4 Error estimation

TRANSP is unfortunately not able to propagate errors through its calculations and has therefore no output for error bars. They are however necessary to assess how robust our calculations are.

If we assume for example, that T_e and T_i measurements both have an error of 10%, then run TRANSP several times for a given discharge, and always vary the two quantities in every possible combination, we get a solid estimate of how errors from T_e and T_i propagate to the output of interest [28]. For this thesis, a simpler and shorter sensitivity study was performed. For one example discharge, T_e and T_i , as well as the edge temperature ratio T_e/T_i and hydrogen minority concentration were varied within a reasonable range. The errors in T_i and in the hydrogen minority concentrations proved to be the dominating error sources for $Q_{i,edge}$. Figure 27 shows a linear correlation between T_i and $Q_{i,edge}$, and that a variation of about 10% leads to a variation of about 13% in $Q_{i,edge}$.

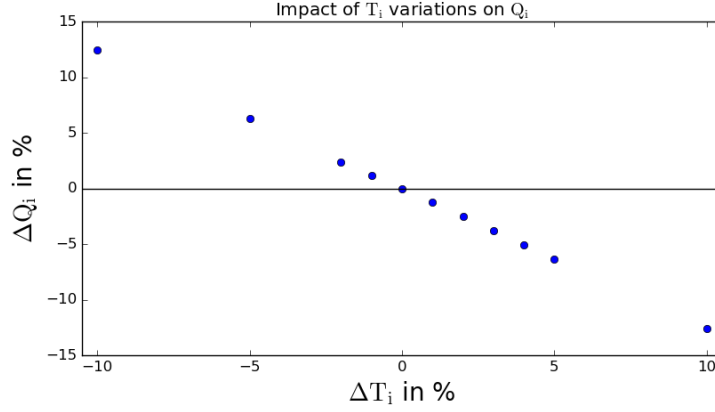


Figure 27: Deviation from $Q_{i,edge}$ with varying T_i for an example discharge.

The hydrogen concentration was constrained to 5% for all TRANSP runs. This value is reasonable for C-Mod discharges. Nevertheless, the concentration can vary and a reasonable estimate for this error seems to be $\pm 3\%$. The error in hydrogen concentration leads to an error in $Q_{i,edge}$ of about 5% (see figure 28).

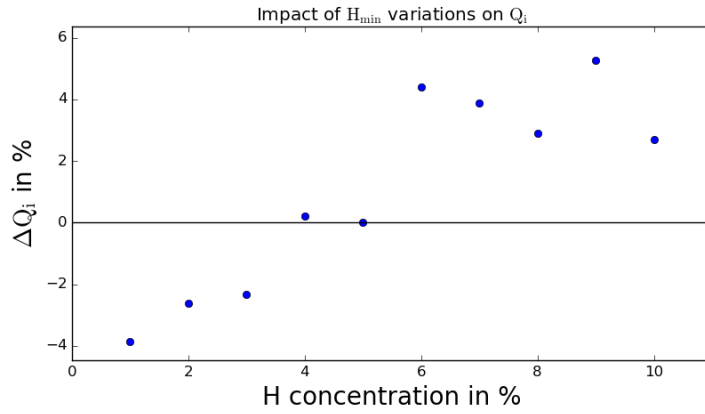


Figure 28: Deviation from $Q_{i,edge}$ with varying hydrogen concentration for an example discharge.

Figure 27 and 28 illustrate how errors from a diagnostic can propagate into the calculated ion heat flux. However, this is not a complete sensitivity study, since all other parameters were fixed in these calculations. A sensitivity study conducted at AUG indicates a similar

behavior for AUG TRANSP-runs. A complete study would be very time consuming and for that reason was not performed for this thesis. Another way to estimate the error bars is to analytically propagate the errors from the diagnostic [28]. For the ion heat flux, that was done in [35] and resulted in an error of 25%.

6.5 Q_i at the L-H transition

The goal of this thesis was to find a relationship between $Q_{i,edge}$ just before a L-H transition and \bar{n}_e similar to equation 11. The method presented in the previous section was applied to several discharges covering the low density branch. Figure 29 shows a clear linear relationship between surface integrated ion heat flux and line averaged density, similar to the AUG results in figure 15, but with more scattering around the fit. This scattering is probably due to the strong coupling in the high density plasmas in C-Mod. For better visibility, only one of the data points has an example error bar. The grey points show the threshold power $P_{L-H,loss}$ with the power threshold fit from [33] to guide the eye and make it easier to compare to previous results. For convenience the index 'loss' is left out from here on.

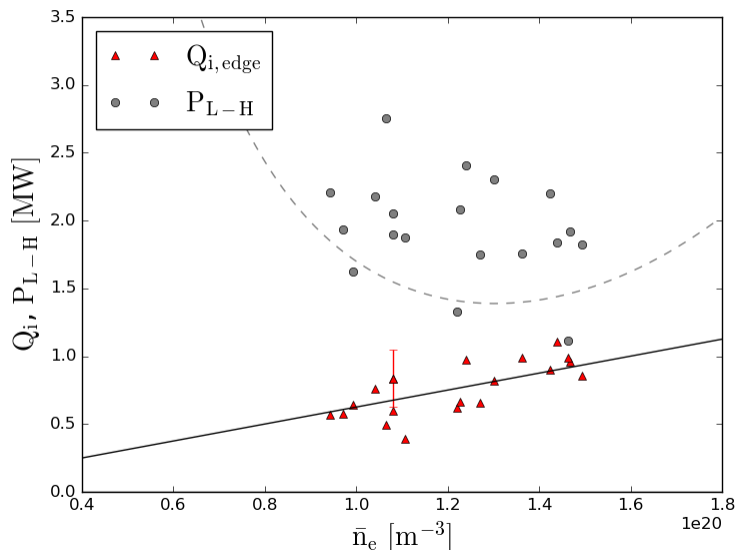


Figure 29: $Q_{i,edge}$ (red) and P_{L-H} (gray) versus density \bar{n}_e in $[m^{-3}]$, just before the L-H transition with $B_T = 5.4T$ and $I_P = 0.9MA$.

This data set gives us a relationship for C-Mod similar to equation 11 that reads

$$Q_{i,edge}^{L-H,fit} = 0.0626\bar{n}_e \quad (28)$$

again with $Q_{i,edge}^{L-H,fit}$ in MW and \bar{n}_e in 10^{19}m^{-3} . This equation will be further discussed in a later section.

6.6 Influence of the different divertor configurations

While all the shots had the same magnetic field and plasma current, they did not all use the same divertor configuration. Figure 30 illustrates the slot divertor configuration on the left hand side and the vertical divertor configuration on the right hand side. In red we see the separatrix, i.e. the last closed flux surface. The point where the magnetic field lines of the separatrix intersect, is the so called X-point and the two points where they meet the wall are referred to as inner and outer strike point. The outer strike point in the slot divertor configuration meets the wall at the bottom of the divertor slot and in the vertical divertor configuration it hits the vertical plates of the divertor.

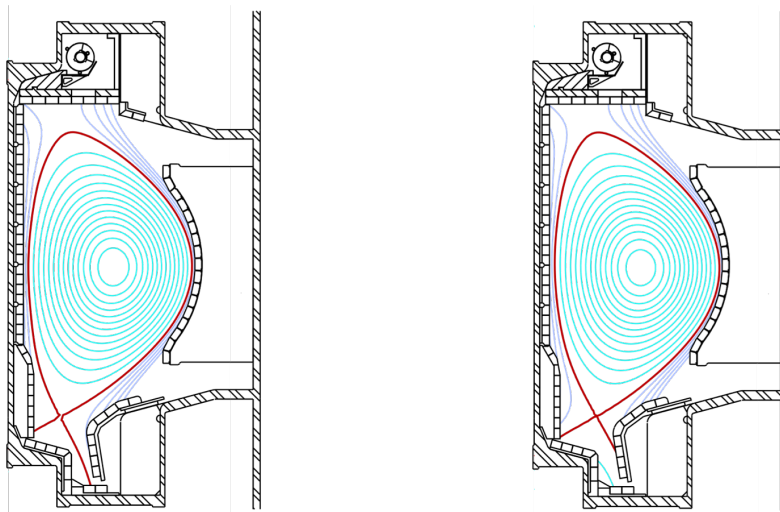


Figure 30: The two divertor configuration used in the discharges presented in this thesis. On the left hand side, we see the outer strike point meeting the wall at the bottom of the divertor slot, hence it is referred to as slot divertor configuration. On the right hand side, the outer strike point is on the vertical divertor plate, hence vertical divertor configuration.

As mentioned in section 5.2, the L-H threshold power is lower for the slot divertor configuration. Figure 31 shows that the slot divertor shots in our data set exhibit the same behavior and tend to be lower than P_{L-H} with the vertical plate divertor (see also figure 32). Intuitively, that should affect $Q_{i,edge}$, since the different divertor conditions could effect the edge density gradient and therefore the L-H-transition [36]. However, in our dataset no clear distinction can be seen in $Q_{i,edge}$ regarding divertor conditions. In the middle of the dataset, there are three blue points from the slot divertor experiments, that lie distinctly below the red triangles in the same density region. The blue points with the lowest and highest densities do not seem to stand out among the red triangles. All in all, considering the small number of data points and large error bars, any difference that might be due to the divertor configuration is probably small and lost in the scatter of the data.

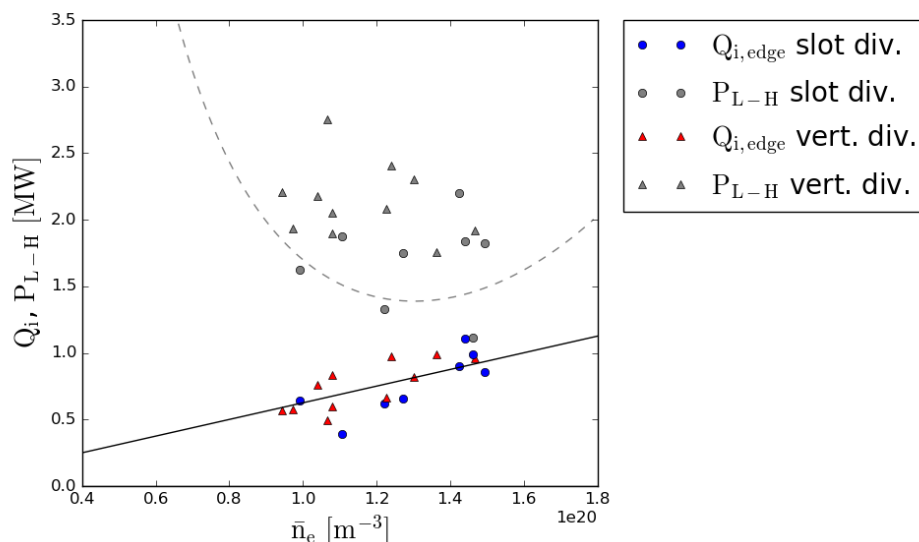


Figure 31: $Q_{i,edge}$ versus density \bar{n}_e in $[m^{-3}]$ just before the L-H-transition with $B_T = 5.4T$ and $I_P = 0.9MA$. Circles mark discharges with a slot divertor configuration, triangles represent discharges with a vertical plate divertor.

To further investigate the impact of the divertor configuration, figure 32 shows a plot of P_{L-H} versus $Q_{i,edge}$. While the difference in total heating power is fairly obvious, there is no visible distinctions in ion heat flux in this figure.

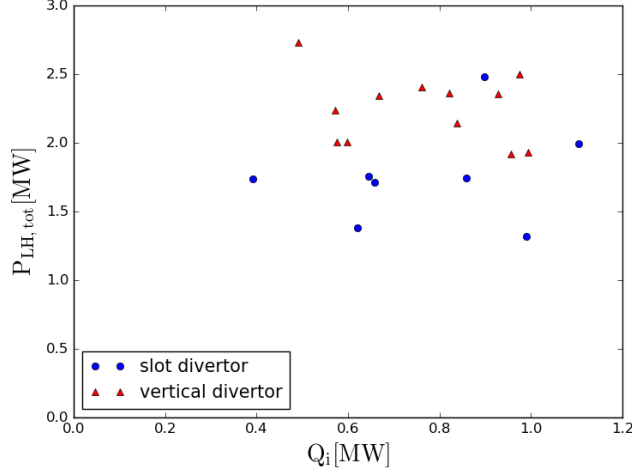


Figure 32: P_{L-H} versus $Q_{i,edge}$ just before the L-H-transition with $B_T = 5.4T$ and $I_P = 0.9MA$. The blue circles mark shots with a slot divertor configuration, red triangles represent shots with a vertical plate divertor.

Instead of looking at the total surface integrated heat flux, we can try to find any influence of the divertor configuration on the contributions from Q_{ie} and $P_{i,ich}$. Figure 33 shows the relative contribution each component makes to the critical edge ion heat flux. The discharges with a slot divertor configuration tend to get a larger portion of $Q_{i,edge}$ from heat exchange. The vertical divertor discharges predominantly get more than 50% of their edge ion heat flux from the auxiliary power that flows into the ion channel.

However, we also have to keep the density dependence of the two contributions in mind, which is why figure 34 shows the integrated ICRH power deposition into the ion channel and the integrated heat exchange against line average density. The slot and vertical divertor discharges are again shown as blue circles and red triangles. We can see that most slot divertor discharges come from the medium and high density range of our set, which explains the tendency to get more power from the heat exchange. The vertical divertor shots are mostly from the lower density range and due to weaker coupling get less power from the heat exchange term which explains the trend from figure 33.

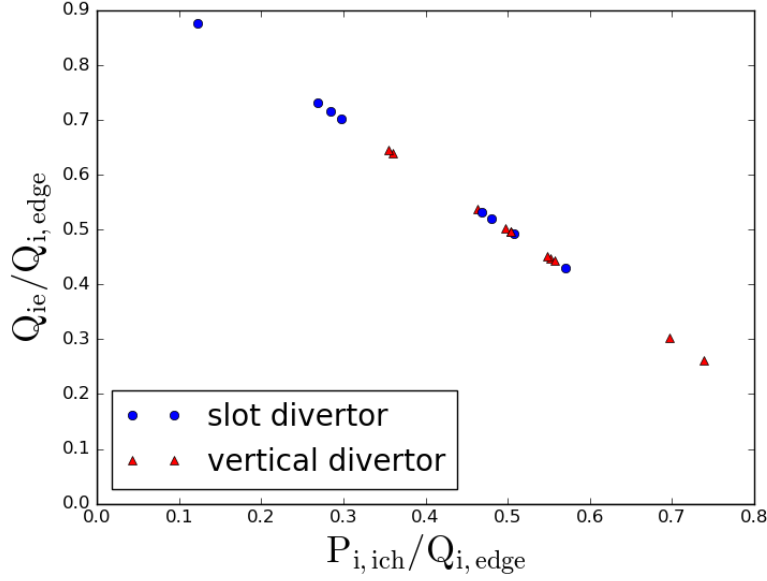


Figure 33: Integrated ICRH power deposition into the ion channel and the integrated heat exchange from the discharges in figure 29 normalized to $Q_{i,edge}$ and plotted against each other. The blue circles mark discharges with a slot divertor configuration, red triangles represent shots with a vertical plate divertor.

In figure 34a) we see that the three slot points we noted in figure 31, get significantly less power from the ICRH than the other points. This could indicate that some issue with the TRANSP input data from these three discharges had a serious effect on the TORIC calculations. However, since the slot divertor configuration has an influence on the edge gradient and ICRH power is deposited in the core, the low $P_{i,ich}$ from these discharges should have nothing to do with the divertor configuration. Aside from these three points, $P_{i,ich}$ tends to rise ever so slightly with density, without any obvious influence of the divertor configuration. The integrated heat exchange scatters a lot more, but we clearly see that Q_{ie} increases with density. Though again, we see no obvious distinction between the two divertor configurations.

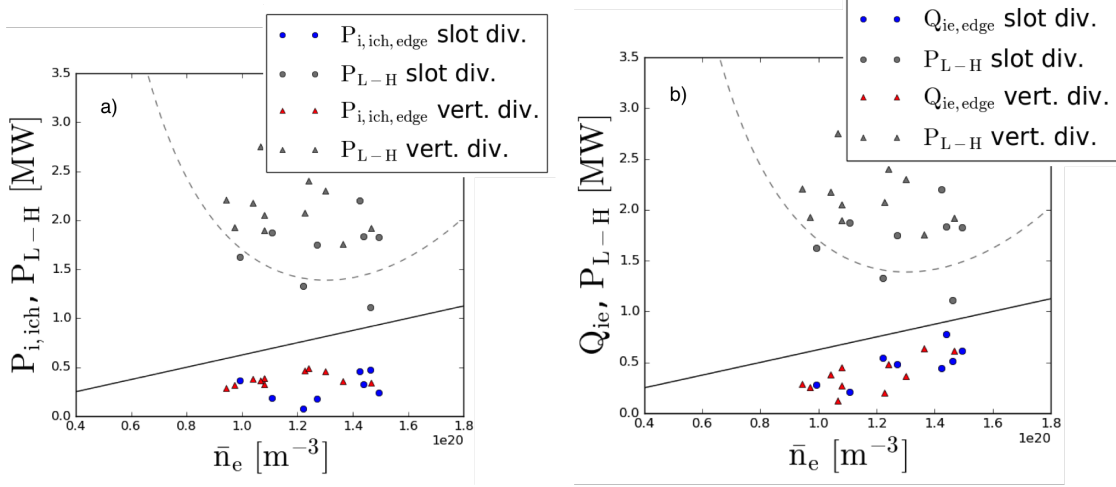


Figure 34: a) ICRF heating power into the ion channel and b) electron-ion heat exchange both versus density. Blue circles and red triangles mark discharges with slot or vertical divertor configuration. In grey, the respective threshold powers and in black ion heat flux fit from equation 28.

So, all in all, even though a different divertor configuration would affect the edge density gradient, and consequently the pressure gradient responsible for E_r , we do not see an effect on the critical edge ion heat flux. Any effect the divertor configuration might have, is lost in the scatter of the data.

6.7 Q_e at the L-H transition

For the sake of completeness, figure 35 shows the edge electron heat flux versus density. While Q_i consists only of the heat exchange and ICRH power that goes directly into the ion channel, equation 18 tells us that Q_e also depends on Ohmic power and the losses due to radiation. The method to calculate Q_e is similar to Q_i although if we look back at figure 19, we see that significantly more power from the ICRH goes directly into the electron channel.

The edge electron heat flux is plotted against density in figure 35. At low densities, a significant fraction of P_{L-H} goes in the electrons only. An increase in density leads to a stronger electron-ion coupling resulting in a more efficient heat exchange. So we know that at higher densities, less heating power is needed for an L-H transition and more heat flows from the electron channel into the ion channel. Consequentially, $Q_{e,edge}$ decreases faster

with density than P_{L-H} . The scatter in $Q_{e,edge}$ is a result of the scatter in radiated power, which is also the reason why P_{L-H} scatters.

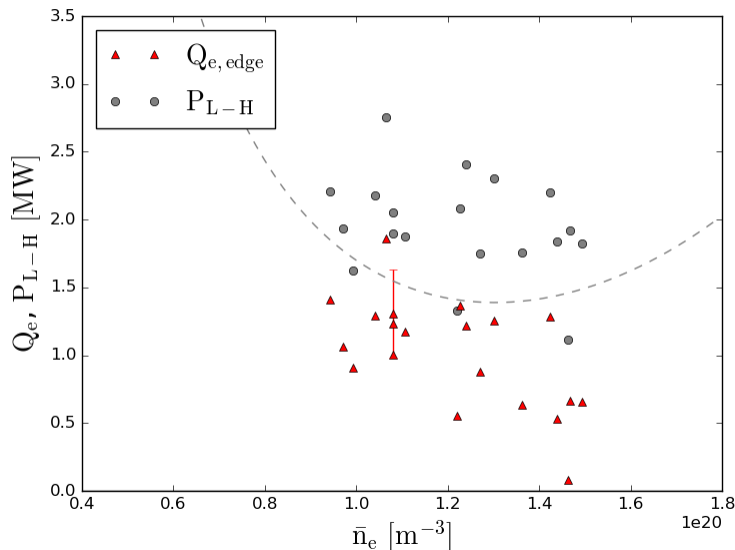


Figure 35: $Q_{e,edge}$ (red) and P_{L-H} (gray) versus density \bar{n}_e in $[m^{-3}]$ just before the L-H transition with $B_T = 5.4T$ and $I_P = 0.9MA$.

6.8 Combining C-Mod and AUG results

Similar to the results from AUG, the surface integrated edge ion heat flux $Q_{i,edge}$ increases linearly with line average density. It appears that to access H-mode on C-Mod, a critical value of edge ion heat flux is required.

Equations 11 and 28 describe the linear behavior of $Q_{i,edge}$ in AUG and C-Mod, which is easily compared to the total heating power P_{loss} . However, we have to keep in mind, that the actual quantity responsible for a L-H transition is $q_{i,edge} = Q_{i,edge}/S$ with the plasma surface S . So to compare the two equations we have to consider the different plasma surface areas.

Another aspect to pay attention to is the different B_T of the AUG data and the C-Mod discharges presented in this thesis. The power threshold law in equation 26 depends on $B_T^{0.8}$

and it seems reasonable, that $q_{i,edge}$ also depends on B_T ⁶. The AUG data was collected with a magnetic field of 2.35T and the data from C-Mod used 5.4T.

So if we take the slope from AUG in equation 11 and take the different plasma surface areas ($S_{AUG} = 44m^2$ and $S_{C-Mod} = 7m^2$) into account and assume a linear dependency on B_T we can correct the slope to C-Mod dimensions

$$0.18 \frac{B_{T,C-Mod}}{B_{T,AUG}} \frac{S_{C-Mod}}{S_{AUG}} = 0.0658 \quad (29)$$

The corrected slope from this equation is surprisingly close to the fit in equation 28. This remarkably good result then allows to formulate a general scaling law for the surface integrated edge ion heat flux and the actual edge ion heat flux necessary for an L-H transition:

$$Q_{i,edge}^{L-H} = a_q B_T S \bar{n}_e \quad (30)$$

$$q_{i,edge}^{L-H} = a_q B_T \bar{n}_e \quad (31)$$

with $Q_{i,edge}^{L-H}$ in MW, $q_{i,edge}^{L-H}$ in MWm⁻², B_T in T, S in m² and \bar{n}_e in 10¹⁹m⁻³. The factor a_q is

$$a_q \approx 1.7 * 10^{-3} \left[\frac{MWm}{T} \right] \quad (32)$$

Equation 31 now needs to be compared with simulated ITER scenarios. Also further investigations of the magnetic field dependency of the critical ion heat flux are required to see whether the assumption of linear scaling with B_T is true.

⁶Another look at the ExB flows (see equation 6) also indicates a magnetic field dependency

$$\left| \frac{\vec{E} \times \vec{B}}{B^2} \right|_{crit} \sim \frac{E_{r,crit}}{B} \sim \frac{\nabla T_{i,crit}}{B} \sim \frac{q_{i,crit}}{n \chi B}$$

6.9 Predictions for ITER

Using the equations from the previous section we can estimate the edge ion heat flux necessary for an L-H transition in ITER. ITER will have a plasma surface of approximately $S = 680m^2$ and a magnetic field of $B_T = 5.3T$ [37]. The predicted density for minimal threshold power in ITER is approximately $\bar{n}_{e,min} = 4 * 10^{19}m^{-3}$ [32]. With these parameters, equation 31 predicts a critical edge ion heat flux of

$$^{ITER}q_{i,edge}^{L-H} \approx 38kWm^{-2} \quad (33)$$

To compare that to the available heating power we use the surface integrated ion heat flux, $^{ITER}Q_{i,edge}^{L-H} \approx 26MW$, which is about half the predicted threshold power and well below the envisioned heating power of $73MW$. So we can predict, that H-mode access in ITER should be possible within the planed operational parameter.

7 Summary and conclusion

In H-mode, a plasma exhibits an improved energy and particle confinement due to reduced turbulent transport at the plasma edge. H-Mode is also the planned operational regime for ITER. To access H-mode, the heating power has to overcome a certain power threshold. This power threshold is described by the scaling law in equation 26 and depends on density, magnetic field and plasma surface.

Previous research conducted at ASDEX Upgrade showed evidence that the edge ion heat flux plays a critical role for L-H transitions. While the power threshold depends non-monotonically on density and exhibits a U-shape, the edge ion heat flux rises linearly with density. So it seems that a critical ion heat flux per particle is required for a L-H transition. To further test this hypothesis, the edge ion heat flux was calculated for selected discharges from Alcator C-Mod. Reactors from the Alcator series were designed to explore the high field approach to nuclear fusion. C-Mod is much smaller than AUG and is able to reach much higher magnetic fields. It can therefore operate in density regions that are usually an order of magnitude higher than densities in ASDEX Upgrade plasmas. So all parameters relevant for P_{L-H} are different from the ones from AUG.

Selected discharges were analyzed with time dependent power balance using the transport code TRANSP. Similar to ASDEX Upgrade, the electron-ion heat exchange played a major role for the ion heat flux. All discharges had a magnetic field of 5.4T, a plasma current of 0.9MA and came from the low to medium density range. ICRH was used as auxiliary heating source and predominantly heated the electrons, which again underlines the importance of the heat exchange from the electron channel into the ion channel.

A major problem for calculating the ion heat flux was, that due to the high density the separation of ion and electron channel was very difficult. That and some diagnostic issues led to some constraints on the TRANSP calculations. Despite all these issues, the analysis yields a result that is remarkably similar to the one from AUG. Even though we see a lot more scatter in the data, the edge ion heat flux just before a L-H transition increases linearly with density.

The scattering and the larger error bars are a result of the high collisionality in C-Mod plasmas, however, we need to point out how remarkable this result is, because of the significant differences of AUG and C-Mod.

The collected discharges used either a slot or a vertical divertor configuration. Previous research at C-Mod had shown that the power threshold was lower for discharges with a

slot divertor configuration. This was confirmed in our analysis, however, the ion heat flux at the L-H transition does not seem to depend on the divertor configuration. If there is a difference, it is probably lost in the scatter.

Comparing the results from C-Mod and AUG led to a linear scaling law to describe the critical edge ion heat flux, depending on the magnetic field and line average density:

$$q_{i,edge}^{L-H} = a_q B_T \bar{n}_e \quad (34)$$

The linear dependance on B_T is an assumption, which needs further investigations. With this scaling law, we can estimate a critical edge ion heat flux for H-mode access in ITER of approximately $38 kW m^{-2}$. With the envisioned heating power, ITER should be able to reach this value and we can therefore predict that H-mode in ITER will be possible.

The analysis of I-mode transitions started, but unfortunately there was not enough time to produce results. This topic will be left for future investigations.

References

- [1] Josef Schweinzer. Physikalische Grundlagen des Kernfusionsreaktors. Vorlesungsnummer 134.750, 2013.
- [2] G. Kamelander. Grundlagen der Plasmatheorie mit besonderer Berücksichtigung der Fusionsphysik. Technische Universität Wien, Vorlesungsnummer 134.359.
- [3] John Wesson and David J Campbell. *Tokamaks*, volume 149. Oxford University Press, 2 edition, 1997.
- [4] Matthias Willensdorfer. *Temporal behavior of the plasma edge density throughout the LH transition in ASDEX Upgrade*. PhD thesis, Vienna University of Technology, 2013.
- [5] Markus Weiland. *Influence of RF heating and MHD instabilities on the fast-ion distribution in ASDEX Upgrade*. PhD thesis, Ludwig-Maximilians-Universität München, 2016.
- [6] John D Lawson. Some criteria for a power producing thermonuclear reactor. *Proceedings of the Physical Society. Section B*, 70(1):6, 1957.
- [7] RA Pitts, S Carpentier, F Escourbiac, T Hirai, V Komarov, AS Kukushkin, S Lisgo, A Loarte, M Merola, R Mitteau, et al. Physics basis and design of the ITER plasma-facing components. *Journal of Nuclear Materials*, 415(1):S957–S964, 2011.
- [8] NP Basse, A Dominguez, EM Edlund, CL Fiore, RS Granetz, AE Hubbard, JW Hughes, IH Hutchinson, JH Irby, B LaBombard, et al. Diagnostic systems on Alcator C-Mod. *Fusion Science and Technology*, 51(3):476–507, 2007.
- [9] F Wagner, G Becker, K Behringer, D Campbell, A Eberhagen, W Engelhardt, G Fussmann, O Gehre, J Gernhardt, G v Gierke, et al. Regime of improved confinement and high beta in neutral-beam-heated divertor discharges of the ASDEX tokamak. *Physical Review Letters*, 49(19):1408, 1982.
- [10] F Wagner. A quarter-century of H-mode studies. *Plasma Physics and Controlled Fusion*, 49(12B):B1, 2007.
- [11] K Itoh, S-I Itoh, and A Fukuyama. The impact of improved confinement on fusion research. *Fusion engineering and design*, 15(4):297–308, 1991.

- [12] F Ryter, R Fischer, JC Fuchs, T Happel, RM McDermott, E Viezzer, E Wolfrum, L Barrera Orte, M Bernert, A Burckhart, et al. I-mode studies at ASDEX Upgrade: LI and IH transitions, pedestal and confinement properties. *Nuclear Fusion*, 57(1):016004, 2016.
- [13] AE Hubbard, T Osborne, F Ryter, M Austin, L Barrera Orte, RM Churchill, I Cziegler, M Fenstermacher, R Fischer, S Gerhardt, et al. Multi-device studies of pedestal physics and confinement in the I-mode regime. *Nuclear Fusion*, 56(8):086003, 2016.
- [14] F Ryter, T Pütterich, M Reich, A Scarabosio, E Wolfrum, R Fischer, M Gemisic Adamov, N Hicks, B Kurzan, C Maggi, et al. H-mode threshold and confinement in helium and deuterium in ASDEX Upgrade. *Nuclear Fusion*, 49(6):062003, 2009.
- [15] F Ryter, SK Rathgeber, L Barrera Orte, M Bernert, GD Conway, R Fischer, T Happel, B Kurzan, RM McDermott, A Scarabosio, et al. Survey of the H-mode power threshold and transition physics studies in ASDEX Upgrade. *Nuclear Fusion*, 53(11):113003, 2013.
- [16] F Ryter, M Cavedon, T Happel, RM McDermott, E Viezzer, GD Conway, R Fischer, B Kurzan, T Pütterich, G Tardini, et al. LH transition physics in hydrogen and deuterium: key role of the edge radial electric field and ion heat flux. *Plasma Physics and Controlled Fusion*, 58(1):014007, 2015.
- [17] E Viezzer, T Pütterich, GD Conway, R Dux, T Happel, JC Fuchs, RM McDermott, F Ryter, B Sieglin, W Suttrop, et al. High-accuracy characterization of the edge radial electric field at ASDEX Upgrade. *Nuclear Fusion*, 53(5):053005, 2013.
- [18] Alexei Pankin, Douglas McCune, Robert Andre, Glenn Bateman, and Arnold Kritz. The tokamak monte carlo fast ion module nubeam in the national transport code collaboration library. *Computer Physics Communications*, 159(3):157–184, 2004.
- [19] Marco Brambilla. Numerical simulation of ion cyclotron waves in tokamak plasmas. *Plasma Physics and Controlled Fusion*, 41(1):1, 1999.
- [20] Miklos Porkolab. Plasma heating by fast magnetosonic waves in tokamaks. In *AIP Conference Proceedings*, pages 99–99. IOP INSTITUTE OF PHYSICS PUBLISHING LTD, 1994.

- [21] Joel C Hosea. Foundations of icrf heating: A historical perspective. In *Advances in plasma physics*, volume 314, pages 128–139. AIP Publishing, 1994.
- [22] IH Hutchinson. Principles of plasma diagnostics. *Plasma Physics and Controlled Fusion*, 44(12):2603, 2002.
- [23] John Sheffield, Dustin Froula, Siegfried H Glenzer, and Neville C Luhmann Jr. *Plasma scattering of electromagnetic radiation: theory and measurement techniques*. Academic press, 2010.
- [24] JW Hughes, DA Mossessian, AE Hubbard, ES Marmar, D Johnson, and D Simon. High-resolution edge thomson scattering measurements on the alcator c-mod tokamak. *Review of Scientific Instruments*, 72(1):1107–1110, 2001.
- [25] JW Hughes, D Mossessian, K Zhurovich, M DeMaria, K Jensen, and A Hubbard. Thomson scattering upgrades on Alcator C-Mod. *Review of scientific instruments*, 74(3):1667–1670, 2003.
- [26] ML Reinke, YA Podpaly, M Bitter, IH Hutchinson, JE Rice, L Delgado-Aparicio, C Gao, M Greenwald, K Hill, NT Howard, et al. X-ray imaging crystal spectroscopy for use in plasma transport research. *Review of Scientific Instruments*, 83(11):113504, 2012.
- [27] ML Reinke and IH Hutchinson. Two dimensional radiated power diagnostics on Alcator C-Mod a. *Review of Scientific Instruments*, 79(10):10F306, 2008.
- [28] Jeffrey Marc Schachter. Local transport analysis for the Alcator C-mod tokamak. 1997.
- [29] D. Ely, David; Ernst. *fiTS v1.4.0 User’s Manual*, August 2011.
- [30] YR Martin, T Takizuka, et al. Power requirement for accessing the H-mode in ITER. In *Journal of Physics: Conference Series*, volume 123, page 012033. IOP Publishing, 2008.
- [31] F Ryter, SK Rathgeber, E Viezzer, W Suttrop, A Burckhart, R Fischer, B Kurzan, S Potzel, et al. L-H transition in the presence of magnetic perturbations in ASDEX Upgrade. *Nuclear Fusion*, 52(11):114014, 2012.

- [32] F Ryter, L Barrera Orte, B Kurzan, RM McDermott, G Tardini, E Viezzer, M Bernert, R Fischer, et al. Experimental evidence for the key role of the ion heat channel in the physics of the L-H transition. *Nuclear Fusion*, 54(8):083003, 2014.
- [33] Y Ma, JW Hughes, AE Hubbard, B LaBombard, RM Churchill, T Golfinopolous, N Tsujii, and ES Marmor. Scaling of H-mode threshold power and L-H edge conditions with favourable ion grad-b drift in Alcator C-mod tokamak. *Nuclear Fusion*, 52(2):023010, 2012.
- [34] Y Ma, JW Hughes, AE Hubbard, B LaBombard, and J Terry. H-mode power threshold reduction in a slot-divertor configuration on the Alcator C-mod tokamak. *Plasma Physics and Controlled Fusion*, 54(8):082002, 2012.
- [35] AJ Creely, NT Howard, P Rodriguez-Fernandez, N Cao, AE Hubbard, JW Hughes, JE Rice, AE White, J Candy, GM Staebler, et al. Validation of nonlinear gyrokinetic simulations of L-and I-mode plasmas on Alcator C-Mod. *Physics of Plasmas*, 24(5):056104, 2017.
- [36] L M Shao and et. al. On the role of the edge density profile for the L–H transition power threshold in ASDEX Upgrade. *Plasma Physics and Controlled Fusion*, 58, 2016.
- [37] EJ Doyle, JC DeBoo, JR Ferron, GL Jackson, TC Luce, Masanori Murakami, TH Osborne, J-M Park, PA Politzer, H Reimerdes, et al. Demonstration of ITER operational scenarios on DIII-D. *Nuclear Fusion*, 50(7):075005, 2010.